

Dust Aerosol Characteristics and Shortwave Radiative Impact at a Gobi Desert of Northwest China during the Spring of 2012

Jianrong BI, Jinsen SHI, Yongkun XIE, Yuzhi LIU

Key Laboratory for Semi-Arid Climate Change of the Ministry of Education and College of Atmospheric Sciences, Lanzhou University, Lanzhou, China

Tamio TAKAMURA and Pradeep KHATRI

Center for Environmental Remote Sensing (CEReS), Chiba University, Chiba, Japan

(Manuscript received 31 October 2013, in final form 28 May 2014)

Abstract

The Semi-Arid Climate and Environment Observatory of Lanzhou University (SACOL) project initiated an intensive field experiment on dust aerosols in Dunhuang from April 1 to June 12, 2012. Using sky radiometer measurements and conducting model simulations, we investigated the dust aerosol characteristics and its shortwave radiative impact on the regional climate. The daily averaged optical features of the aerosols markedly varied throughout the study period. High aerosol loading and predominantly coarse particulates were observed in the spring of 2012 ascribed to the influence of prevalent dust storm. The single scattering albedo at 500 nm (SSA_{500}) varied from 0.91 to 0.97 on dusty days and from 0.86 to 0.91 on dust-free days, indicating that the dust aerosols sourced from northwest China were not strongly absorbing. Surface radiation quantities estimated by the radiative transfer model excellently agreed with ground-based and satellite observations, with correlation coefficients exceeding 0.990 and mean differences ranging from -3.9 to 17.0 W m^{-2} . The daily mean aerosol shortwave direct radiative forcing (ARF) values were largely negative at the surface (-79.4 to -3.2 W m^{-2}) and moderately positive in the atmosphere (2.2 – 25.1 W m^{-2}), indicating strong cooling at the surface and moderate atmospheric warming. The monthly averaged ARFEs (ARFs per unit aerosol optical depth at 500 nm (AOD_{500})) at the surface were $(-73.9 \pm 11.6) \text{ W m}^{-2}$, $(-67.4 \pm 8.3) \text{ W m}^{-2}$, and $(-74.4 \pm 5.4) \text{ W m}^{-2}$ in April, May, and June, respectively (overall average of $(-70.8 \pm 7.9) \text{ W m}^{-2}$), comparable to previously obtained values in East Asia and India domains. The relations between the diurnal ARFs at the surface and top of the atmosphere (TOA) and the AOD_{500} indicate that aerosol composition remained relatively stable at Dunhuang during the spring of 2012. The ARF at the TOA was positive for SSA_{500} less than 0.85 or when the imaginary part at 500 nm exceeded 0.015.

Keywords dust aerosol; shortwave radiative forcing; Gobi Desert; radiative closure experiment; single scattering albedo

1. Introduction

As is well known, atmospheric aerosol is a very

important climate forcing factor. Aerosol particles can directly scatter and absorb solar/terrestrial radiation, cooling or warming the Earth–atmosphere system. Meanwhile, as cloud condensation nuclei, they can modify the size and number concentration of cloud droplets and the cloud residence time, besides promoting atmospheric chemical reactions. These modifications exert a profound impact on

Corresponding author: Jianrong Bi, College of Atmospheric Sciences, Lanzhou University, Lanzhou 730000, China

E-mail: bijr@lzu.edu.cn

©2014, Meteorological Society of Japan

the global energy budget and hydrologic cycle of the Earth system (Ackerman et al. 2000; Ramanathan et al. 2001a; Kaufman et al. 2005; Shao et al. 2011). According to the Intergovernmental Panel on Climate Change (IPCC 2007), we currently lack detailed and quantitative knowledge of the optical and microphysical properties, chemical compositions, and spatiotemporal distributions of aerosols. Consequently, the climatic impacts of aerosols remain largely unknown. A comprehensive understanding of aerosol characteristics and radiative forcing is essential for accurately assessing future regional and global climate change. Yu et al. (2006) calculated the global average aerosol direct radiative forcing (ARF) at the surface and top of the atmosphere (TOA) by integrating satellite retrievals with model simulations. They obtained over-land ARFs of $-4.9 \pm 0.7 \text{ W m}^{-2}$ and $-11.8 \pm 1.9 \text{ W m}^{-2}$ at the TOA and surface, respectively. These values are close to the TOA and surface values of $-6.0 \pm 1 \text{ W m}^{-2}$ and $-11.0 \pm 2 \text{ W m}^{-2}$, respectively, reported by Kim and Ramanathan (2008). Nakajima et al. (2003) derived the monthly mean whole sky ARF from various methods, and obtained -8 to -5 W m^{-2} at the TOA and -23 to -10 W m^{-2} at the surface of Gosan and Amami-Oshima sites. However, to form a complete picture of global climate change, the aerosol climatic effect at different regional scales requires further investigation.

East Asia is regarded as one of the world's largest dust source regions. The region emits a huge quantity of mineral dust particulates that are entrained high into the atmosphere (Huang et al. 2007). These particulates are usually transported over thousands of kilometers, even across the Pacific Ocean, by the prevailing westerlies (Uno et al. 2009). East Asia is also a principal industrial area, which compounds its environmental impact (Nakajima et al. 2003). Therefore, to predict the evolution of the climate system, we must account for aerosol radiative forcing and its climatic effect in the East Asia domain. Thus far, a large number of field experiments have been conducted in East Asia (including China) by many investigators (Huebert et al. 2003; Nakajima et al. 2003; Shi et al. 2005; Mikami et al. 2006; Takamura et al. 2007; Li et al. 2007a, 2011; Huang et al. 2008a). These studies are crucial for understanding the climatic effect of aerosols. Several recent publications (Li et al. 2007b, 2010; Xia et al. 2007; Ge et al. 2010) have concluded that although the ARF at the TOA is small or neutral, China sources moderately strong absorptive aerosol, which can heat the atmosphere and cool the surface. Uchiyama et al.

(2005) inferred the single scattering albedo of Aeolian dust from sky radiometer and in situ ground-based measurements. They reported that unpolluted Aeolian dust (sourced from northwest China) is not largely absorbing. Li et al. (2010) pointed out that despite intensive efforts to elucidate the optical properties and radiative forcing of aerosol across China, the northwestern region has been poorly sampled and thus neglected. Huang et al. (2007, 2009) studied the vertical distribution and heating rate of dust aerosol over the Taklimakan Desert, combining the Fu-Liou radiative transfer model with satellite observations. Bi et al. (2011) and Liu et al. (2011) examined the optical and radiative properties of aerosol over the Loess Plateau of northwest China using CIMEL sun photometer and PREDE sky radiometer measurements, respectively. Using multiple Micro-Pulse Lidars, Huang et al. (2010) surveyed the vertical profiles and long-range transport of dust aerosols in northwest China. Wang et al. (2010) characterized the dust plume transport in northwest China by combining in situ measurements with satellite data. Wang et al. (2013) estimated the radiative effect of a heavy dust storm over northwest China during the spring of 2010 using the Fu-Liou model and ground observations. All of these previous investigations provide invaluable insights for our present study.

The Gobi and desert regions over northwest China are among the primary dust aerosol sources in East Asia. To better understand the impact of dust aerosol on climate, the Semi-Arid Climate and Environment Observatory of Lanzhou University (hereinafter referred to as SACOL, <http://climate.lzu.edu.cn/english/>) conducted an intensive field experiment in Dunhuang during the spring of 2012. The ground-based measurements provide the aerosol optical depth (AOD), Ångström exponent ($\alpha_{400-870}$), volume size distribution ($dV/d\ln r$), single scattering albedo (SSA), and asymmetry factor (ASY) of the aerosol particulates. A dozen of the high-precision observations collected by the ground-based radiometers can be compared to surface radiation quantities estimated from the radiative transfer model. The dust aerosol radiative forcing and heating rate are assessed using the model and measured data. This campaign is vital for understanding the characteristics and variations of dust aerosols in the source region, and thereby accurately evaluating the effect of dust aerosol on future global and regional climate change.

This paper summarizes the primary scientific objectives, the field campaign design, and the preliminary findings. Our study focuses on the spring of 2012

when dust storms prevailed over northwest China.

2. Field experiment and measurements

2.1 Field experiment

To improve our understanding of the drought processes and associated climate change in northwest China (Huang et al. 2008b), SACOL initiated and conducted an intensive field campaign on dust aerosol from April 1 to June 12, 2012. This experiment was designed to achieve the following objectives: (1) investigate the microphysical, optical, and chemical properties of dust aerosol in the source region, (2) validate and enhance the inversion products of satellite remote sensing, (3) assess the direct radiative impact of dust aerosol on the regional climate. SACOL's Mobile Facility (SMF) was assembled at Dunhuang farmland (40.492°N, 94.955°E, 1061 m above MSL), a tiny isolated oasis surrounded by Gobi desert and arid areas in northwest China. The site is located in the westernmost end of Hexi Corridor of Gansu province, adjacent to the east margin of Kumtag Desert and approximately 400 km distant from Taklimakan Desert. In addition, the facility is directly downwind of the Taklimakan dust outbreaks and seats at the northeast of Dunhuang city (~70 km distant). Dunhuang city holds a population of 180,000 and its economy is dominated by agriculture and tourism rather than by industry and factories. Hence the dust storms sourced from Dunhuang City are largely free of anthropogenic contamination. Being situated inland and nearby an arid-desert region, Dunhuang experiences an extremely dry climate with much sunshine. The annual mean rainfall is only 42.2 mm, approximately 70 % of which occurs in summer (see Fig. 1, sourced from the China Meteorological Administration), and evaporation reaches up to 2400 mm. The annual mean temperature is 9.5 °C with huge diurnal and annual variations. The annual mean wind speed is approximately 2.0 m s⁻¹, peaking in spring (~2.6 m s⁻¹). On account of its special geographical location and unique land surface, combined with its dry climate and strong wind conditions, Dunhuang is subject to frequent dust storms during the spring and early summer. Therefore, Dunhuang has become an important basic station for studying dust aerosol and has hosted a large number of national and international intensive field experiments, including the Aerosol Characterization Experiment-Asia (ACE-Asia, Huebert et al. 2003), and the Japan-China joint project of Aeolian Dust Experiment on Climate Impact (ADEC, Mikami et al. 2006).

During the SACOL experiment, two mobile

sites were deployed at Dunhuang; the SMF was erected near farmland in the Gobi Desert region, and a set of spectra and broadband radiometers was installed at the top of a three-story building (about 10 m above ground level and 1 km from the SMF). A suite of active and passive ground-based remote sensing instruments was deployed throughout the field campaign; namely, the Micro-Pulse Lidar (MPL), Prede sky radiometer (POM-01), Cimel sun photometer (CE318), EKO grating spectroradiometer (MS-700) and Multi-Filter Rotating Shadowband Radiometer (MFRSR). In situ measurements were collected by an aerosol integrated observing system, whose main components were an Aethalometer (AE-31), a Particle Soot Absorption Photometer (PSAP), a Multi-Angle Absorption Photometer (MAAP), an Ambient Particulate Matter (RP1400a, Thermo), an Aerodynamic Particle Sizer (APS-3321), two TSI three-wavelength nephelometers (TSI-3563, one for PM₁₀ cutting head and other for PM_{2.5}) and a Condensation Particle Counter (CPC 3807). The in situ aerosol instruments and radiometers were purchased and calibrated by factory staff immediately before deployment. Prior to experiment, the sky radiometer was also newly calibrated at the Meteorological Research Institute (MRI; 36.056°N, 140.125°E, 25 m above MSL) in Japan. This experiment provides an excellent opportunity to study the dust aerosol characteristics and its shortwave radiative impact on regional climate over northwest China.

2.2 Sky radiometer measurements

A sun/sky radiometer (Model POM-01, manufactured by PREDE Co. Ltd.) was deployed at Dunhuang throughout the study period. The PREDE sky radiometer is widely used in the SKYNET—aerosol-cloud-radiation interaction ground-based observation network in East Asia (Takamura et al. 2004). An overview of the instrument, and its operation, calibration, and inversion algorithms, are presented in Nakajima et al. (1996). Here we provide a brief description. The sky radiometer (also known as an Aureolemeter) measures the direct solar irradiance and sky diffuse radiance at several standard wavelengths (315, 400, 500, 675, 870, 940, and 1020 nm). Five of the seven channels are used to retrieve the aerosol optical properties. The 315 and 940 nm channels are capable of inferring columnar ozone amount and precipitable water in centimeters, respectively. The half bandwidth of the 315 nm channel is 3 nm; the half bandwidth of the remaining channels is 10 nm. The full angle field of view is 1.0°, and the minimum scattering angle of

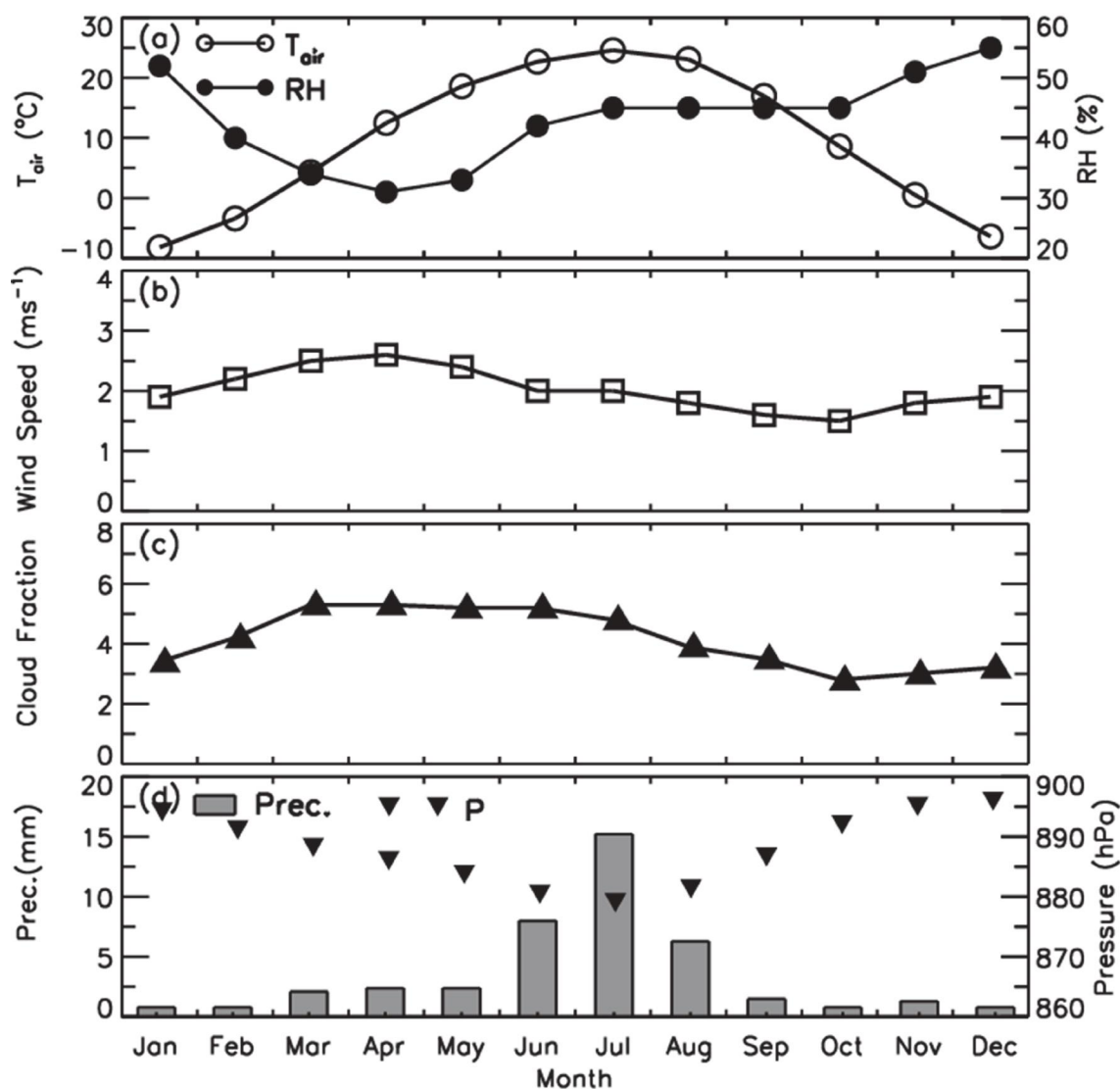


Fig. 1. Monthly averaged values of (a) air temperature (T_{air}) and relative humidity (RH), (b) wind speed, (c) cloud fraction, and (d) precipitation (prec.) and barometric pressure at Dunhuang weather station (No.: 52418, 40.15°N, 94.68°E, 1139 m above MSL). The data sets represent China Climate Standard Value (Year 1971–2000), which are provided by China Meteorological Administration (CMA).

measurement is approximately 3°. The sky radiometer operates only during daytime and collects data regardless of sky conditions. Its dynamic range is 10^7 and the typical measurement interval is 10 minutes. To enable sky radiance almucantar measurements, the instrument is mounted on a vertical-horizontal two-axis mount driven by a digital servo motor.

2.3 Ground-based radiation measurements

As described above, a suite of state-of-the-art

broadband spectral instruments was set up at Dunhuang. These instruments, which acquire solar or shortwave (SW) radiation and terrestrial or long-wave (LW) radiation fluxes, were installed in a row on a standard horizontal platform (approximately 4.0 m above the ground) where the field of view was unobstructed in all directions. The direct normal radiation was independently measured by two normal incidence pyrheliometers (NIP, Eppley Lab. and CHP1, Kipp & Zonen), while diffuse radiation was acquired

from a ventilated and shaded pyranometer (PSP, Eppley Lab.). The pyranometer and pyrhemometers were installed on a two-axis automatic solar tracker (2AP, Kipp & Zonen) with a tracking accuracy of 0.05° . The global solar radiation ($0.285\text{--}2.85\ \mu\text{m}$) was directly measured by a ventilated pyranometer (PSP) and another redundant black-and-white radiometer (B&W 8-48) without a ventilator. The downward LW radiations ($3.5\text{--}50\ \mu\text{m}$) were independently measured by a ventilated and shaded pyrgeometer (PIR) and another ventilated PIR. The thermal offset of the pyranometers during daytime measurements was corrected by considering the IR loss (Bi et al. 2013). All radiation fluxes were time resolved to 1 min and stored in a Campbell data logger. The integrity of the datasets was ensured by adopting the Baseline Surface Radiation Network (BSRN) quality control procedure (Ohmura et al. 1998). Moreover, the total radiation measured by both pyranometers was compared and the global radiation was calculated by summing the solar direct NIP (or CHP1) and the diffuse radiation from PSP measurements. In this way, we could inspect and identify any abnormal data points. Bi et al. (2013) reported that the measurements obtained by the two pyranometers differed within $10\ \text{W m}^{-2}$.

2.4 Total sky imager measurements

A Total Sky Imager (Model TSI-880) was also installed at Dunhuang. This instrument captures high-resolution pictures of the sky at one-minute intervals from sunrise to sunset. It is an automatic, full-color, and digital imaging system that processes data in real time and displays the daytime sky conditions. The images are analyzed by an onboard processor, which computes the fractional cloud cover and sunshine duration by a sophisticated cloud detection algorithm. The results are saved as JPEG files. Users can visit the processed and unprocessed sky images via a web browser interface.

3. Results and methodology

3.1 Retrieval of aerosol optical depth

The monochromatic direct solar irradiance is compliant with Beer-Lambert law, which can be used to compute columnar aerosol optical depth (AOD). The linear form of Beer's law is given by

$$\ln[V(\lambda) \cdot d^2] = \ln[V_0(\lambda)] - \tau(\lambda) \cdot m(\theta) \quad (1)$$

where $V(\lambda)$ denotes the digital voltage measured at the surface for a specific wavelength λ , and $V_0(\lambda)$ is the extraterrestrial voltage at the TOA. The total optical

depth $\tau(\lambda)$ is the sum of the Rayleigh scattering, aerosol extinction, and ozone absorption. θ is the solar zenith angle (in radians) and d is the relative Earth-Sun distance in Astronomical Units (AU) at the time of observation. The relative optical air mass $m(\theta)$ is determined by (Kasten and Young 1989)

$$m(\theta) = \frac{1}{\cos(\theta) + 0.150 \times (93.885 - \theta)^{-1.253}} \quad (2)$$

The calibration constants $V_0(\lambda)$ are usually determined from a logarithmic plot of the optical air mass versus the measured direct solar irradiance (a Langley plot). The total optical depth $\tau(\lambda)$ is obtained from Eq. (1). The atmospheric aerosol optical depth (τ_a) is then computed by subtracting the Rayleigh (τ_R) and ozone (τ_{O_3}) components from the total optical depth:

$$\tau_a = \tau - \tau_R - \tau_{O_3} \quad (3)$$

The Rayleigh scattering and ozone absorption contributions are given by (Liou 2002)

$$\tau_R = 0.00864 / \lambda^{(3.916 + 0.074 \times \lambda + 0.050 / \lambda)} \times P_S / P_0$$

$$\tau_{O_3} = K_{O_3} \times O_3,$$

where P_S is the local surface barometric pressure measured by a WXT-520 sensor (Vaisala, Finland), and P_0 is the sea level pressure. K_{O_3} is the ozone absorption coefficient, and O_3 is the columnar ozone amount derived from daily observations by a Total Ozone Mapping Spectrometer (TOMS) (Bhartia et al. 1993).

The columnar aerosol optical properties are extracted from direct solar irradiance and sky diffuse radiance data using the "SKYRAD.pack" (Version 4.2) software code developed by Nakajima et al. (1996). It is worth noting that the calibration constants $V_0(\lambda)$ for the SKYNET sky radiometer data were inferred from an improved Langley plot (ILM; Campanelli et al. 2007), in which the AOD was estimated in advance by an inversion procedure involving the direct solar irradiance and forward scattering radiance data ($3^\circ\text{--}30^\circ$). The calibration constants were then determined by linear best fitting to the $\ln[V(\lambda) \cdot d^2]$ versus $\tau(\lambda) \cdot m(\theta)$ plot given by Eq. (1). On account of its strong performance and straightforward application, the ILM is a widely used in situ calibration procedure. The status of the instrument can be periodically checked by users in the field.

3.2 Cloud screening

To properly elucidate the optical properties of

Table 1. Calibration constants were derived from Normal Langley method based on sky radiometer data at five wavelengths under clear-sky cases.

Date	400 nm 1.00×10^{-5}	500 nm 1.00×10^{-4}	675 nm 1.00×10^{-4}	870 nm 1.00×10^{-4}	1020 nm 1.00×10^{-4}	R ²	Time
April-12	9.502	2.599	3.856	2.941	1.721	0.9998	AM
May-14	9.261	2.550	3.787	2.894	1.674	0.9998	AM
May-14	9.259	2.555	3.798	2.904	1.675	0.9999	PM
May-15	9.121	2.517	3.745	2.866	1.657	0.9999	AM
May-15	9.284	2.574	3.835	2.933	1.689	0.9983	PM
May-29	9.011	2.512	3.746	2.874	1.654	0.9996	AM
May-29	9.137	2.547	3.794	2.907	1.666	0.9998	PM
June-09	9.057	2.528	3.758	2.874	1.652	0.9998	AM
June-09	9.241	2.574	3.820	2.920	1.675	0.9998	PM
May-26	9.163	2.547	3.798	2.912	1.671	0.9995	PM

R² denotes correlation coefficient at 500 nm, AM and PM denote the forenoon and afternoon periods, respectively.

aerosol, the cloud contaminated data must be separated from cloud-free data. To eliminate observations affected by cloud, we here adopt the cloud screening algorithms developed by Smirnov et al. (2000) and Khatri and Takamura (2009). The former approach is mainly based on the principle that the temporal variations of cloud are greater than that of aerosol. Accordingly, diurnal stability check, smoothness criteria and three standard deviation criteria are applied to cloud screening. Furthermore, the criteria of testing with global radiation data and spectral variability test for AOD (Khatri and Takamura 2009) are utilized in this article as well.

3.3 Calibration results

As mentioned above, the ILM is commonly adopted for in situ calibration of sky radiometer data, especially at typical urban sites. The period of the present study included four completely cloudless days (May 14, 15, 29, and June 9) and three half-days of cloudless skies (April 12, May 26, and June 7). Because of the extremely dry climate, the atmospheric conditions on all of these days were stable, with relatively small aerosol loading and little water vapor (see Fig. 3 for details). Under these conditions, we may infer the calibration coefficients from the normal Langley (NL) plot rather than the ILM. The NL method assumes a highly stable atmosphere with relatively low AOD conditions throughout the calibration period, which are clearly satisfied at the Dunhuang site. In this paper, we present the calibration outcomes of two completely clear-sky days; additional outcomes are summarized in Table 1.

Figure 2 depicts the NL calibration results of sky

radiometer data collected at five wavelengths on May 14 and 29, 2012. Regardless of wavelength, very little difference is observed between morning and afternoon calibrations. At all wavelengths, optimized linear fitting yields a very strong correlation with few outliers, as shown in the figure. Specifically, the correlation coefficients of the NL plot at 500 nm exceed 0.998, regardless of time (AM versus PM) and date (See Table 1). In the current study, we rejected data points yielding correlation coefficients below 0.995 for five wavelengths. Having carefully examined the calculated calibration constants, we assigned a unique V_0 value to each wavelength over the entire study period. We then used Beer's law to calculate the AOD from the direct sun irradiance data at different wavelengths.

3.4 Aerosol microphysical and optical properties

This subsection focuses on the diurnal and daily variations of the aerosol characteristics (namely, the AOD, Ångström exponent, SSA, and volume size distribution) extracted from sky radiometer measurements throughout the study period.

Figure 3 displays the diurnal AOD variation at five wavelengths on four completely clear-sky days (May 14, 15, 29, and June 9, 2012), derived from the PREDE sky radiometer. Although frequent dust storms strike Dunhuang during springtime, the AOD values are very low even under clear-sky conditions. These results may reflect the low background level of aerosol loading, itself attributable to small anthropogenic input and the extremely dry conditions. All background AOD levels were at or below 0.12 (ranging from 0.03–0.12). The AOD remained rela-

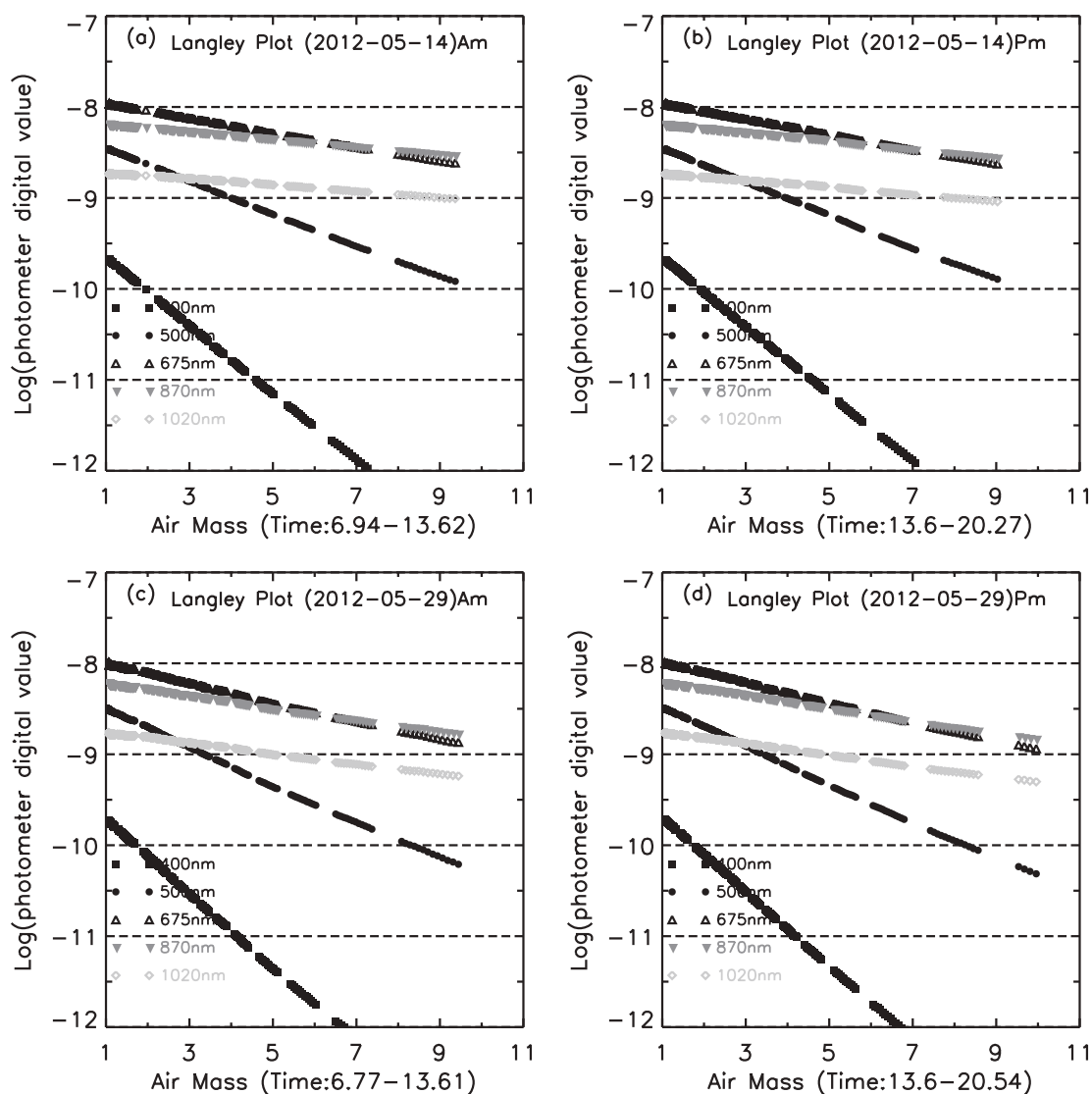


Fig. 2. Calibration results were derived from Normal Langley method based on sky radiometer data at five wavelengths on May 14 and 29, 2012.

tively stable throughout the daytime on May 14 and 29, ideally satisfying the assumptions of the Langley plot. Bi et al. (2013), who examined seven cloudless days with background aerosol loading in Badain Jaran Desert, northwest China, reported that the AOD_{500} values varied from 0.04 to 0.08 on June 17, 2010. The results of this article are comparable to the annual mean AOD of 0.029 recorded at Nam Co observatory in the central Tibetan Plateau (Xia et al. 2011).

Figure 4 delineates the time series of AOD at five wavelengths during April (top), May (center), and

June (bottom), extracted from sky radiometer data. The AOD exhibits the same temporal trend regardless of channel, implying that the NL-derived calibration constants are reliable. Abnormally high AOD values were observed on some days in April. In June, the AOD values were relatively low (<0.6) and stable with all cases less than 0.6.

The Ångström wavelength exponent α is obtained from a log-log plot of AOD (τ_a) versus wavelength (λ). To determine α , we conducted log-linear fittings of data obtained at four wavelengths in the 400–870 nm range, i.e., at $\lambda = 0.40, 0.50, 0.675$, and $0.87 \mu\text{m}$.

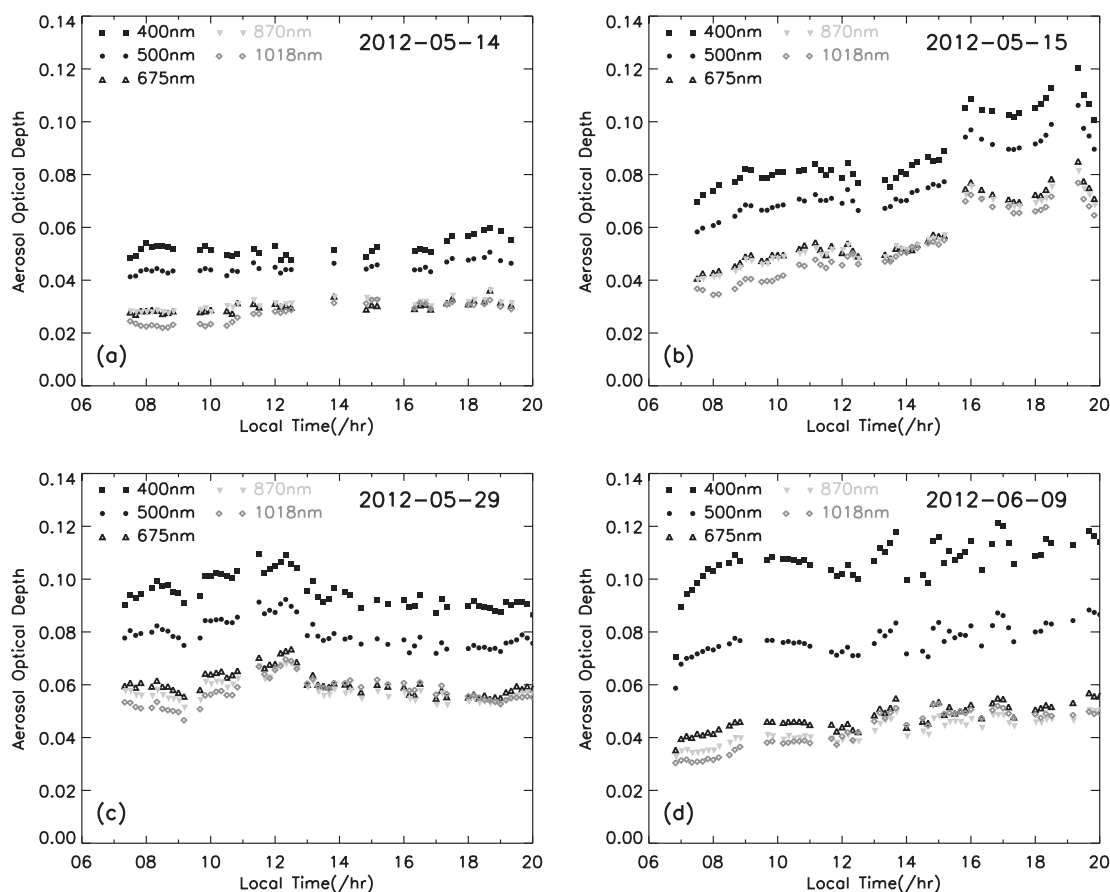


Fig. 3. Diurnal variation of aerosol optical depth (AOD) at five wavelengths under four completely clear-sky days from sky radiometer measurements.

α is commonly used to describe the spectral dependence of τ_a and to estimate the aerosol size distribution (Eck et al. 1999). For instance, small α around zero represents large dust particles; conversely, a large α (~ 2.0) indicates small particles (Dubovik et al. 2002b). The relationship between the instantaneous $\alpha_{400-870}$ and AOD_{500} during the spring of 2012 is plotted in Fig. 5. Throughout the three spring months, a similar negative relationship appears between $\alpha_{400-870}$ and AOD_{500} . From Fig. 5a, we observe that 84 % of the $\alpha_{400-870}$ values are below 0.5 and that $\alpha_{400-870}$ varies from -0.01 – 0.86 over a wide range of AOD_{500} values (0.07 – 1.56). The opposite trend appears in June; that is, a broad range of $\alpha_{400-870}$ (0.12 – 1.49) is observed over a narrow AOD_{500} range (0.06 – 0.5). Throughout May, the $\alpha_{400-870}$ ranges over a moderate-to-low range of AOD_{500} values.

The aerosol single scattering albedo (SSA) is the ratio of the aerosol scattering coefficient to the total

extinction coefficient (scattering plus absorption). The SSA characterizes the absorption properties of aerosols and is an important quantity in evaluating aerosol radiative forcing. The asymmetry factor (ASY) is the first moment of the cosine of the particle scattered radiation angular distribution. In cloud free atmospheres, ASY varies from 0.1 under pristine conditions to 0.75 in heavily polluted environments (Zege et al. 1991).

Dubovik et al. (2002a) emphasized that nonspherical dust particles greatly affect the accurate retrieval of aerosol characteristics. The real part of the complex refractive index of nonspherical particles is underestimated in most investigations of Mie scattering, artificially increasing the fine-particle mode. The spherical particle assumption also significantly affects the retrieved phase function. However, the SSA can be accurately retrieved by inverting the sun and sky radiance data in the whole almucantar. In addition,

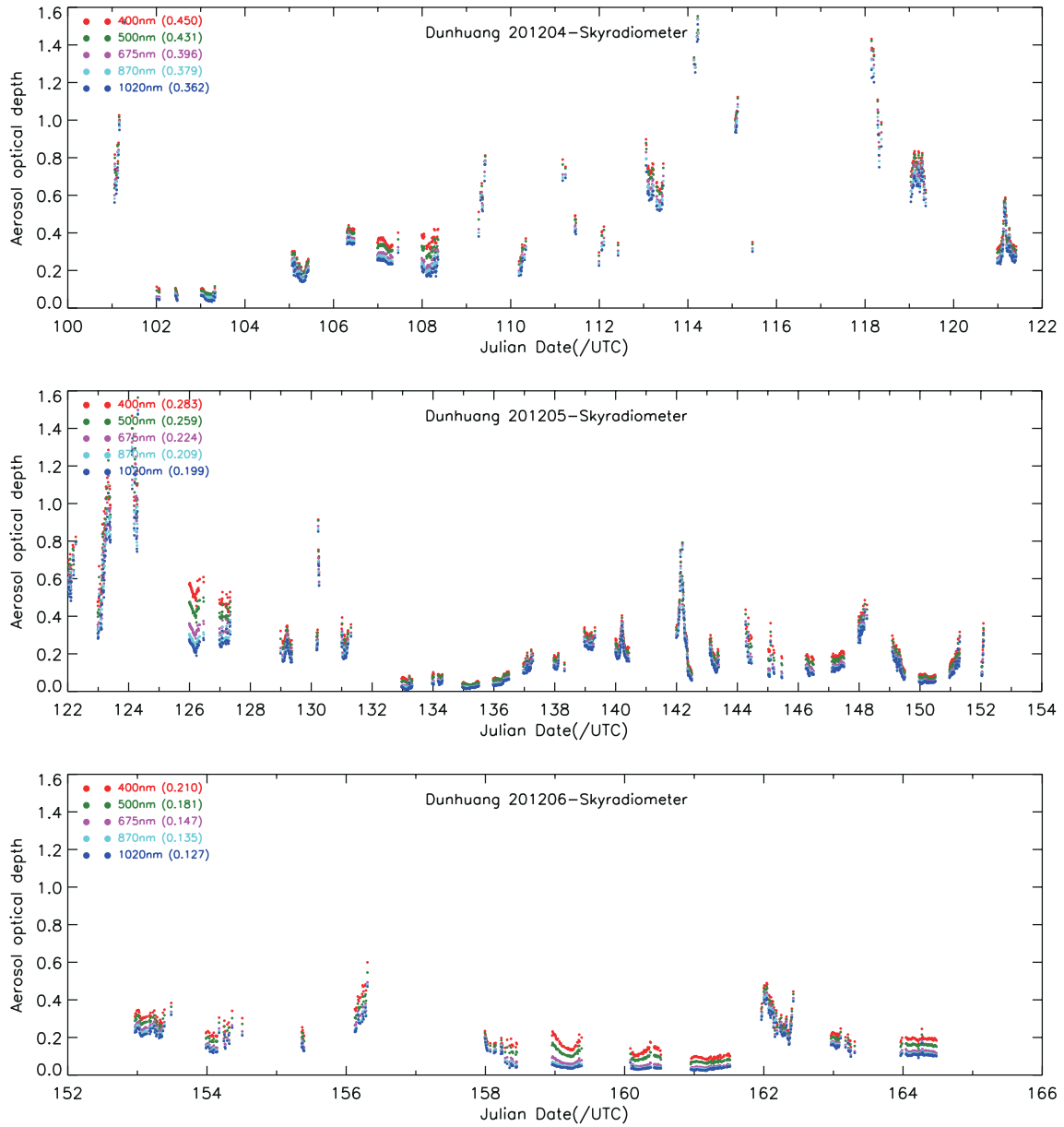


Fig. 4. Time series of aerosol optical depth (AOD) at five wavelengths for April (top), May (center), and June (bottom) from sky radiometer measurements.

the modeling results of Yang et al. (2007) and Mishchenko et al. (1997) verified that particle nonsphericity can substantially change the scattering phase function, but exerts little impact on the total optical cross section, SSA and ASY. Nevertheless, nonsphericity is an essential consideration in accurate retrieval of large dust particles.

Figure 6 illustrates the daily means of AOD₅₀₀,

$\alpha_{400-870}$, SSA₅₀₀, and ASY₅₀₀ throughout the Dunhuang study period. All parameters vary widely on a daily basis. The daily mean AOD₅₀₀ continuously increases throughout April, reflecting incursion by dust particles. The atmospheric conditions in April are rather turbid; the AOD₅₀₀ exceeds 0.4 in 50 % of the days in that month. The atmosphere clears in May and June; in these months, the AOD₅₀₀ is typically less

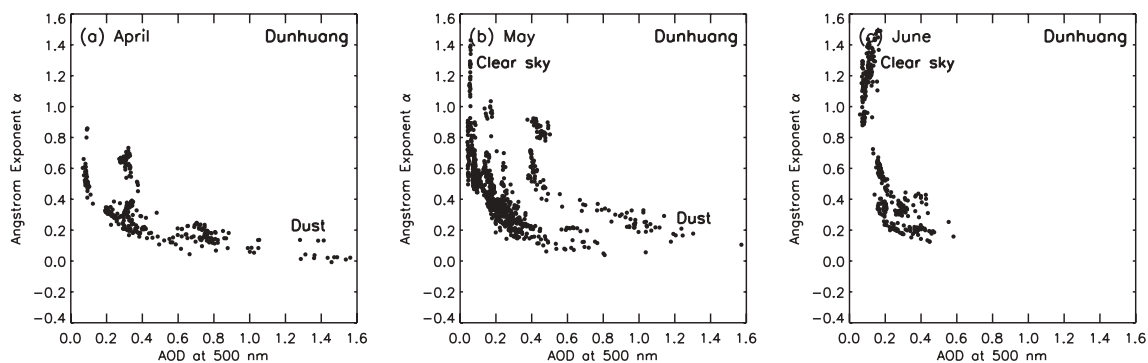


Fig. 5. Relationships between the instantaneous Ångström exponent versus aerosol optical depth at 500 nm for (a) April, (b) May, and (c) June, 2012.

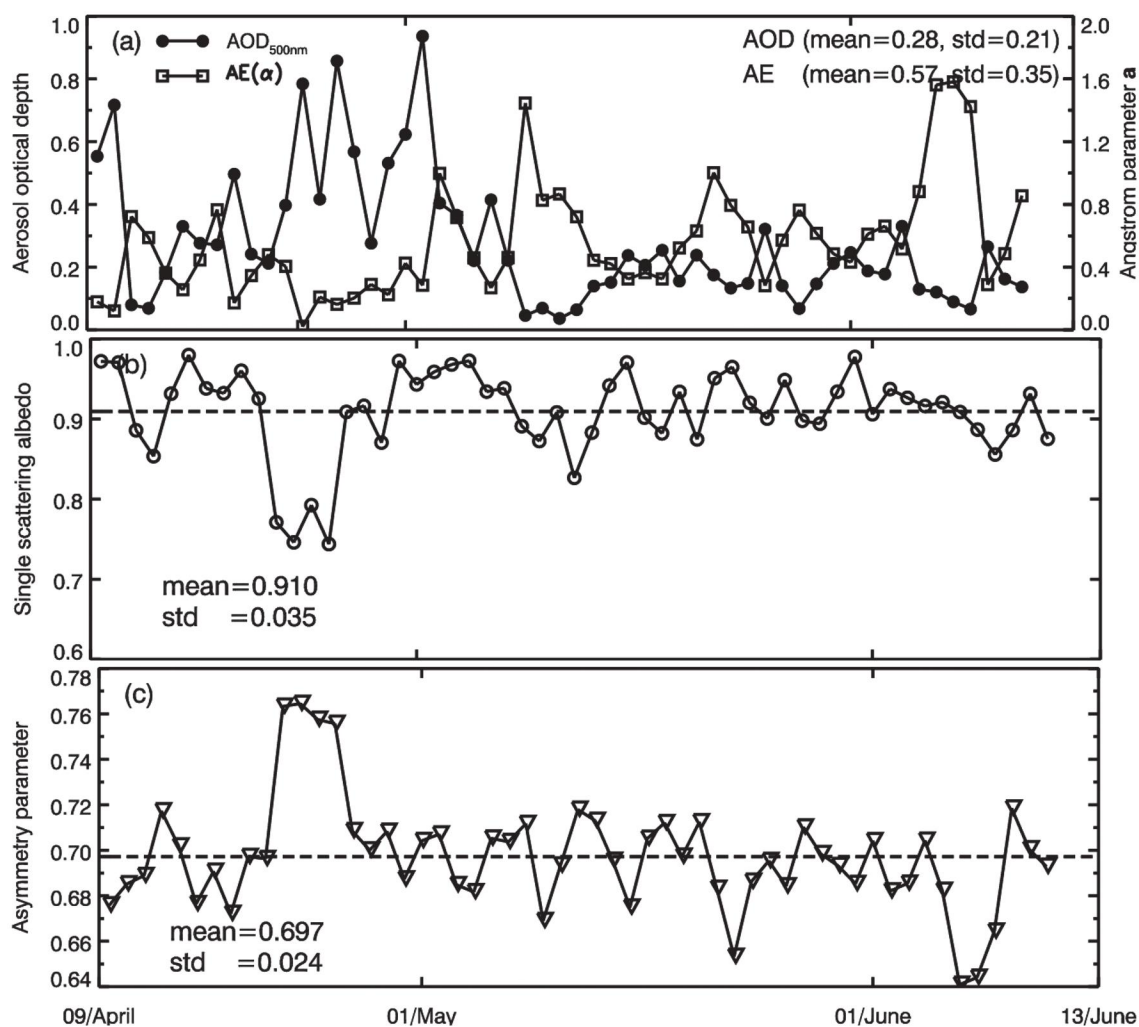


Fig. 6. Daily means of (a) aerosol optical depth (AOD) at 500 nm and Ångström exponent (400–870 nm), (b) single scattering albedo, and (c) asymmetry factor at 500 nm during the whole period.

than 0.3. The daily average AOD₅₀₀ is distinctly negatively correlated with $\alpha_{400-870}$ (see Fig. 6a), implying that when the daily mean AOD₅₀₀ increases the $\alpha_{400-870}$ decreases, and vice versa. This result is anticipated because larger AODs tend to be associated with larger dust particles (i.e., smaller α). The AOD₅₀₀ values range from 0.04 to 0.94, while the $\alpha_{400-870}$ vary from 0.02 to 1.58. The total average AOD₅₀₀ and $\alpha_{400-870}$ are 0.28 ± 0.21 and 0.57 ± 0.35 respectively, consistent with the multi-year mean results of Gao et al. (2013). The single-scattering albedo and asymmetry factor at 500 nm (i.e., SSA₅₀₀ and ASY₅₀₀) range from 0.74 to 0.98 and from 0.64 to 0.76 respectively, with respective means of 0.909 ± 0.035 and 0.697 ± 0.024 . Hansen et al. (1997) demonstrated that, the key value of SSA for cooling or heating the global mean surface temperature was 0.86 for fixed clouds. Bi et al. (2011, 2013) suggested that the seasonal mean SSAs of aerosol vary within 0.87–0.96 over Loess Plateau and within 0.83–0.98 in Badain Jaran Desert, northwest China. Kim et al. (2005) reported similar SSAs for aerosols in East Asia (i.e., 0.89 for Asian dusts in Dunhuang, 0.9 for urban aerosols in Yinchuan, and 0.88 for biomass-burning aerosols in Sri-Samrong). Using data collected from a particle soot absorption photometer (PSAP) and a nephelometer (M903), Uchiyama et al. (2005) obtained SSA values between 0.91 and 0.93 at Qira (37.0°N, 80.7°E), located in the Taklimakan Desert of northwest China. All of these results are consistent with the results of our present study. By contrast, the SSA₅₀₀ is much lower at Zhangye (0.75 ± 0.02 ; Ge et al. 2010) and over India (0.74 – 0.84 ; Pandithurai et al. 2008).

Figure 7 shows scatterplots of the daily mean SSA₅₀₀ versus the AOD₅₀₀ and the Ångström exponent (400–870 nm). The SSA₅₀₀ tends to slightly increase and decrease with increasing AOD₅₀₀ and Ångström exponent, respectively. Li et al. (2007b) attributed these phenomena to different species of aerosol emitted from various sources, such as coarse-mode soil desert dust, fine-mode smoke, and pollution. Therefore, if the aerosol composition is fixed, additional dust particles will enhance the scattering (increasing the AOD), weaken the absorption efficiency (increasing the SSA), and increase the particle size (decreasing the AE).

The columnar aerosol volume size distribution (dV/dlnr) was retrieved by combining direct sun and sky radiance measurements. Retrieval algorithms have been published by Kaufman et al. (1994) and Nakajima et al. (1996). Here we adopt a linear and nonlinear inversion scheme. Furthermore, the

“SKYRAD.pack” software assumes that aerosols comprise spherical and homogeneous particles. The errors in the retrieved dV/dlnr are generally larger for small and large particles than for mid-radius particles. Nakajima et al. (1996) claimed that the accuracy of dV/dlnr was within 20 % for intermediate sized particles, but deteriorated to 35 %–100 % at the edges particle size. To eliminate the artificially high dV/dlnr obtained at small and large radii ($r < 0.03 \mu\text{m}$ and $r > 7 \mu\text{m}$, respectively), we imposed a threshold condition (Yang et al. 2009), under which the mean volume values at the limits of the size range must be smaller than the mean value of the entire spectral size distribution. According to the observational data, the maximum value of a normal particle size distribution is generally below $0.1 \mu\text{m}^3 \mu\text{m}^{-2}$. Therefore, abnormal data with absolute values 10 times larger than this benchmark (exceeding $1.0 \mu\text{m}^3 \mu\text{m}^{-2}$) are filtered out. Such outliers normally arise from cloud contamination. In fact, throughout the study period, the size distribution of heavy dust was maximized at $0.87 \mu\text{m}^3 \mu\text{m}^{-2}$ (see Table 2); therefore, the imposed $1.0 \mu\text{m}^3 \mu\text{m}^{-2}$ threshold is reasonable.

Figures 8a–c show the daily mean of the retrieved aerosol size distributions (dV/dlnr) in April, May, and June. The dV/dlnr presents an overall bimodal pattern with a 0.1 – $0.2 \mu\text{m}$ fine particle mode and a 1.69 – $2.5 \mu\text{m}$ coarse particle mode. The dust aerosol increases the coarse-particle fraction in April relative to its May and June proportions. Figure 8d depicts the corresponding monthly average aerosol size distributions. Again, all months show a bimodal structure, with a fine-particle mode at 0.2 – $0.3 \mu\text{m}$ and a coarse-particle mode at 2 – $4 \mu\text{m}$. These distributions vary according to changes in the amplitude and spectral dependence of AOD. The volume distribution of the coarse-particle mode dramatically varies, whereas that of the fine fraction remains comparatively stable. This suggests that aerosol comprises mainly coarse particles during the Dunhuang spring. The magnitude and shape of the coarse-particle mode distinctly changes throughout April, largely reflecting intrusion by dust particles. The volume concentration ratio of coarse to fine mode particles (C_v/C_{vf}) in April (namely, 20) is very close to the spring mean of ~ 20 obtained in a 1999–2000 Dunhuang study (Xia et al. 2004), but greater than that obtained at a Zhangye site (~ 10) in a semi-desert region of northwest China (Ge et al. 2010), and much smaller than in the Sahara desert domain (~ 50) (Dubovik et al. 2002b). We also linked high fractions of coarse-mode particles to high AOD values and low Ångström exponents (See Fig. 8d).

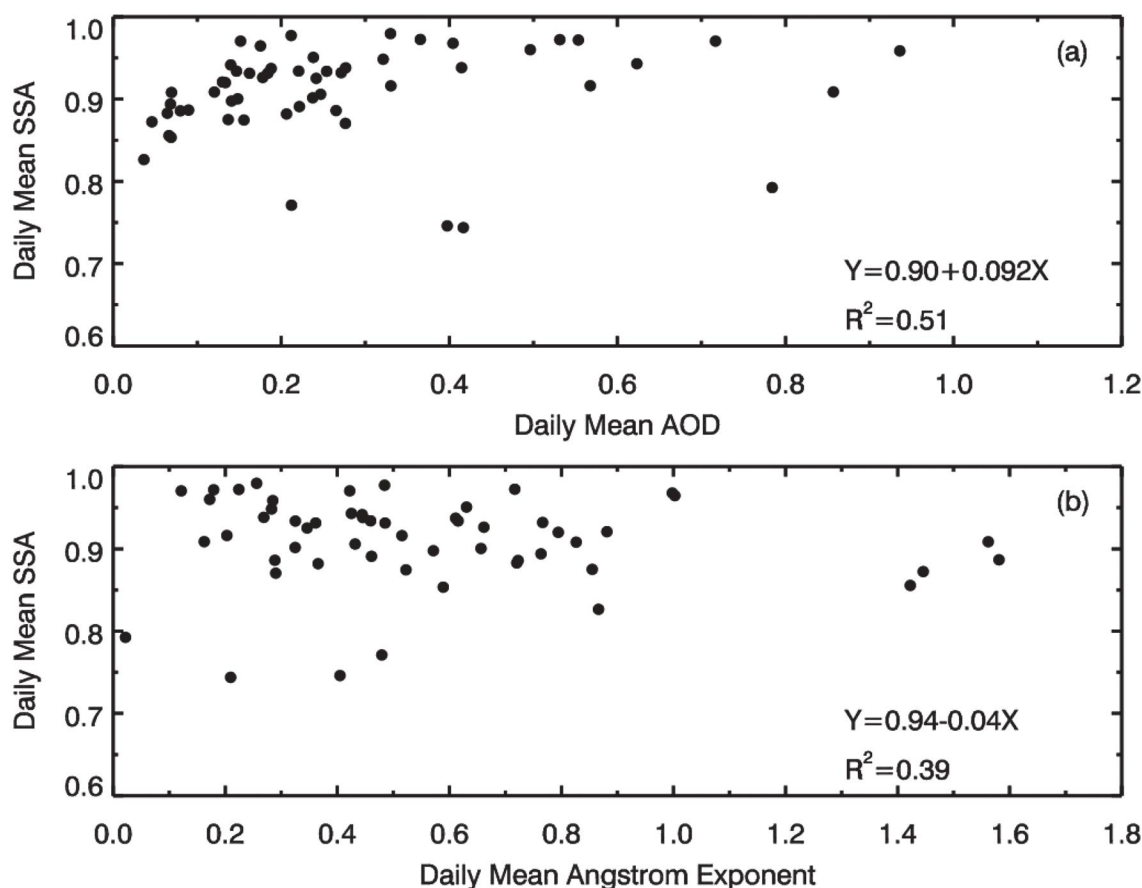


Fig. 7. Daily means of single scattering albedo at 500 nm versus (a) AOD₅₀₀ and (b) Ångström exponent (400–870 nm).

Table 2. Volume size distributions under diverse weather conditions

	Heavy dust		Flowing dust		Clear sky	
	Fine	Coarse	Fine	Coarse	Fine	Coarse
radius (μm)	0.17	5.29	0.17	1.69	0.17	2.47
$dV/d\ln r$ ($\mu\text{m}^3 \mu\text{m}^{-2}$)	0.009	0.87	0.007	0.12	0.004	0.014

4. Aerosol shortwave radiative forcing

4.1 Radiative transfer model

The Santa Barbara Discrete-ordinate Atmospheric Radiative Transfer model (SBDART), created by the University of California in Santa Barbara (Ricchiazzi et al. 1998), computes plane-parallel radiative quantities in the Earth's atmosphere and at the

surface under cloudless and cloudy conditions. This software code incorporates all important processes affecting the ultraviolet, visible, and infrared radiation fields. The SBDART model determines the radiation fluxes at a single point location. Bi et al. (2013) have confirmed that the broadband spectrum irradiance simulated by SBDART favorably agrees with measurements (to within 3 %). The important input

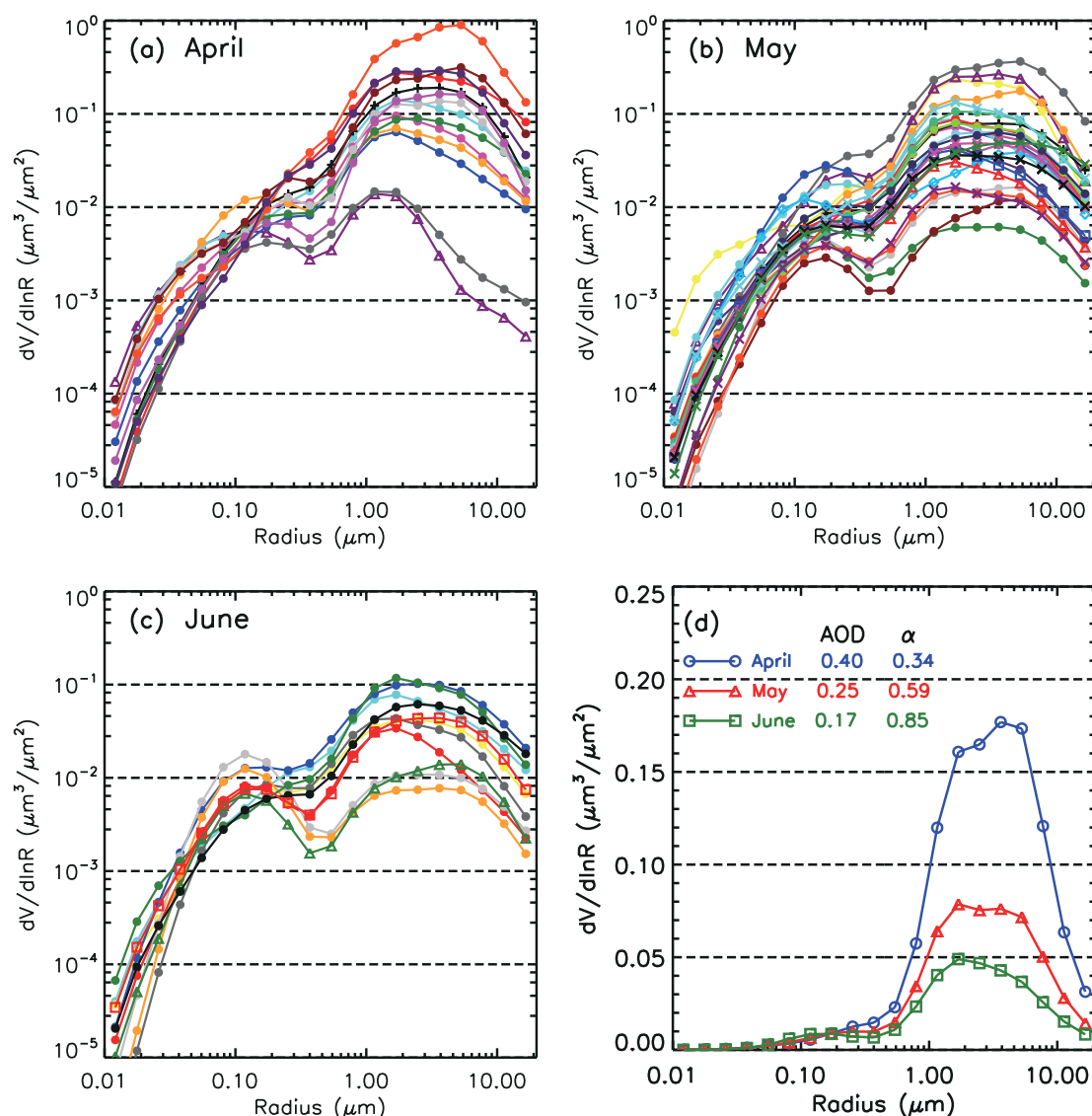


Fig. 8. Daily means of aerosol volume size distributions during (a) April, (b) May, and (c) June, and (d) monthly averaged aerosol volume size distribution during the spring of 2012 at Dunhuang.

parameters are AOD, SSA, ASY, and their wavelength dependences of spectral variations, the column precipitable water vapor, total ozone amounts, and spectral surface albedo. In this paper, the aerosol optical features at 400, 500, 675, 870, and 1020 nm, and also the Ångström exponent, were retrieved from the sky radiometer. The AODs were extrapolated beyond the measured wavelengths using the Ångström formula. The SSAs and ASYs at the other channels were interpolated and extrapolated by combining the observations with a continental pollution model (OPAC,

denoting Optical Properties of Aerosols and Clouds) (Hess et al. 1998). The temperature, pressure, and relative humidity vertical profiles up to a height of approximately 12 km were measured by a radiosonde launched at a nearby location. Above this altitude, the standard mid-latitude summer atmospheric profiles were filled up (Bi et al. 2013). The present article adopts the daily mean radiosonde profiles in the model. The daily total ozone amount was extracted from an Ozone Monitoring Instrument (OMI, NASA Aura mission), ranging from 297 to 366 DU in our

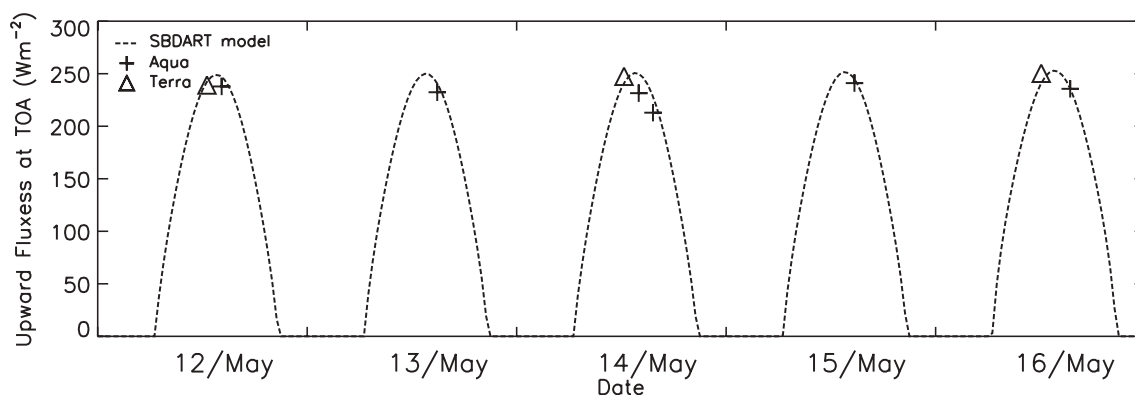


Fig. 9. Model-simulated (dotted lines) and CERES-Aqua (cross)/Terra (triangle) observed upward solar broadband fluxes (0.30–5.0 μm) at TOA. The valid CERES values are obtained within a box of $\pm 0.3^\circ$ in latitude and longitude centered on the Dunhuang site.

case. The broadband surface albedo (0.3 throughout the study period), was based on data recorded by the Clouds and Earth's Radiant Energy System (CERES) satellite. The spectrally dependent surface reflectance at Dunhuang was deduced from the Moderate Resolution Imaging Spectroradiometer (MODIS) bidirectional reflectance distribution function/Albedo products, which resolves to 500 m (Moody et al. 2005). MODIS provides both black-sky albedo (BSA)-direct reflectance and white-sky albedo (WSA)-bihemispherical reflectance at seven spectral bands (0.47, 0.555, 0.659, 0.858, 1.24, 1.64, and 2.10 μm) as well as three broad bands (0.4–0.7, 0.7–3.0, and 0.4–3.0 μm). Finally, we determined the fractions of soil, vegetation, and water as 95 %, 4 %, and 1 %, respectively. The surface solar radiation fluxes at spectral wavelengths ranging from 0.28 to 2.85 μm were calculated using the SBDART model.

4.2 Comparison between model and measurement

Before evaluating the aerosol direct radiative forcing, we first inspected the accuracy of the parameters in a radiative closure experiment. Figure 9 outlines the upward solar broadband fluxes at the TOA (0.3–5.0 μm) simulated by SBDART (dotted lines) and observed by CERES-Aqua (crosses)/Terra (triangles). The valid CERES satellite values were calculated within a box of 30 km \times 30 km ($\pm 0.3^\circ$) centered on the Dunhuang site. Here we compared the clear-sky cases only when the Aqua/Terra satellite passed over the location. The modeled instantaneous TOA fluxes agree with the CERES measurements within 10 W m^{-2} , confirming the reliability of the input parameters of spectral surface reflectance and

broadband surface albedo.

Figure 10 compares the simulated and ground-based observed solar radiation fluxes at Dunhuang. The global solar radiation is calculated by adding the diffuse radiation to the product of the direct solar radiation and the cosine of the solar zenith angle. The total solar radiation acquired directly from the PSP pyranometer is also compared with the simulated results (Fig. 10d), although the uncertainty in these measurements is increased at high solar zenith angle because a different detector responds to the solar incident angle. Our results demonstrate excellent radiative closure, and the correlation coefficients exceed 0.990 in all cases. Generally, good consistency between modeled and directly measured radiation implies that the AOD and gas absorption parameters in the model are correct, in both magnitude and spectral dependence. The few divergent points in the diffuse radiation arise from the retrieved uncertainties in the SSA and ASY. However, the good agreement between most of the diffuse radiation data indicates that the retrieved SSA and ASY are also reasonable. The correlation coefficients, mean differences (MED, denoting the mean simulated result minus the mean observed result), and standard deviations range from 0.991 to 0.998, from -3.9 to 17.0 W m^{-2} and from 13.7 to 18.9 W m^{-2} , respectively. The differences are comfortably within the instrumental and model uncertainties and are similar to recently reported results (Bi et al. 2013). From Figs. 10c and 10d, we find that the calculated global radiation is more consistent than direct measurement in this study.

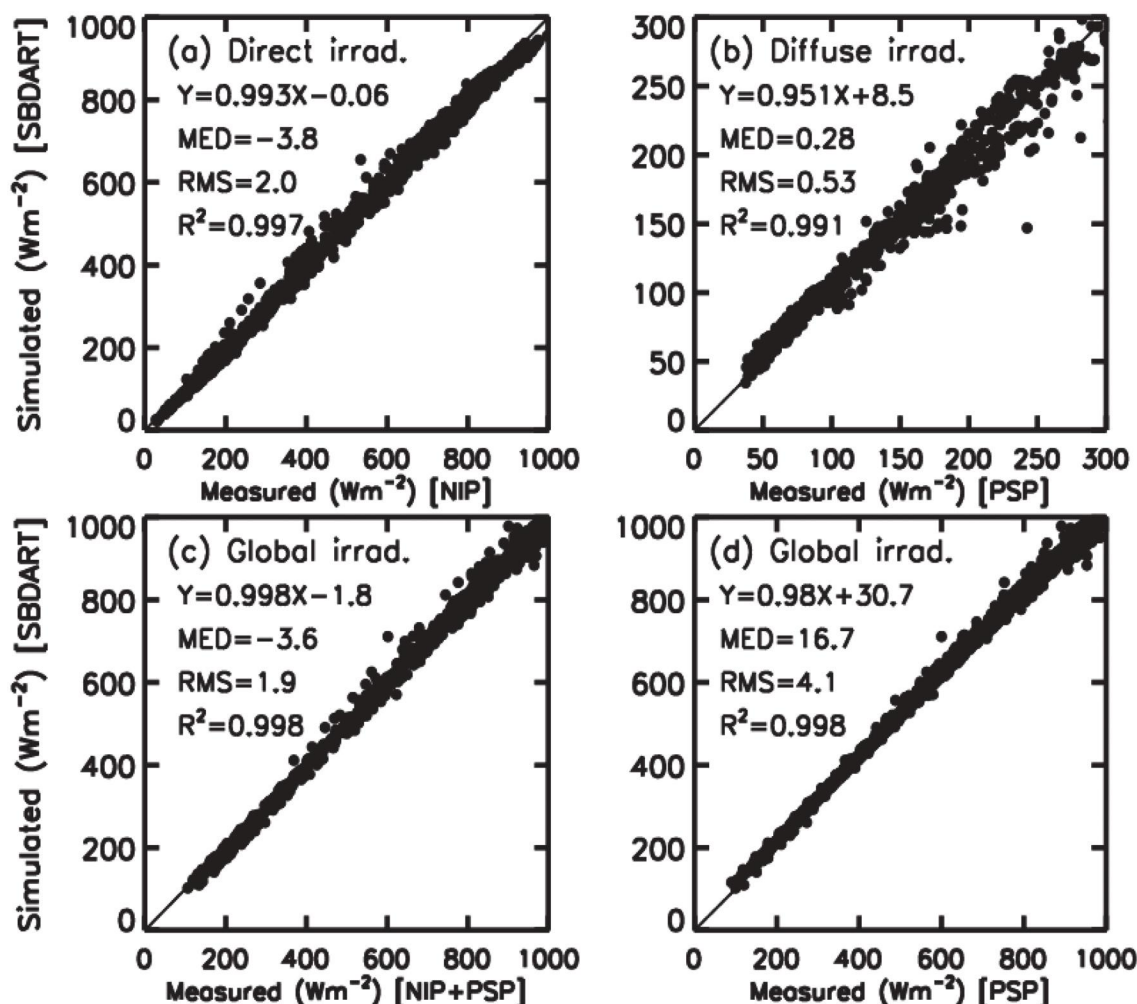


Fig. 10. Comparisons between the SBDART simulated and ground-based measured (a) direct, (b) diffuse, (c) global total from the sum of direct and diffuse irradiances, and (d) directly global irradiances from the unshaded pyranometer during the spring of 2012. The 1:1 line (solid) is shown for comparison.

4.3 Aerosol direct radiative forcing

Aerosol direct radiative forcing (ARF) is defined as the discrepancy between net shortwave radiative fluxes in the presence and absence of aerosol under cloudless conditions. The methodology is detailed in recent papers (Ge et al. 2010; Bi et al. 2013). In the current study, the ARF was derived by combining the model simulations with ground-based measurements. The ARF at the surface depends strongly on aerosol loading and the optical features (such as SSA and ASY). By the abovementioned approach, we first estimated the instantaneous ARF in a 30-minute interval. Next, assuming that the aerosol concentration remains relatively invariant throughout the day, we computed

the 24-hour averaged ARF by interpolating the AOD and optical features across cloudy intervals and intervals of missing data (including nighttime) to generate a continuous time series.

Figure 11 presents the daily mean ARF values at the TOA and surface during April, May, and June, 2012. The atmospheric ARF values were obtained as the ARF at the TOA minus the surface ARF. As shown in Fig. 11, the 24-hour averaged ARFs are largely negative at the surface (-79.4 to -3.2 W m^{-2}) and slightly negative to slightly positive at the TOA (-25.2 to 11.9 W m^{-2}) throughout the entire period, indicating a moderately positive atmospheric ARF (2.2 to 25.1 W m^{-2}). For comparison, the esti-

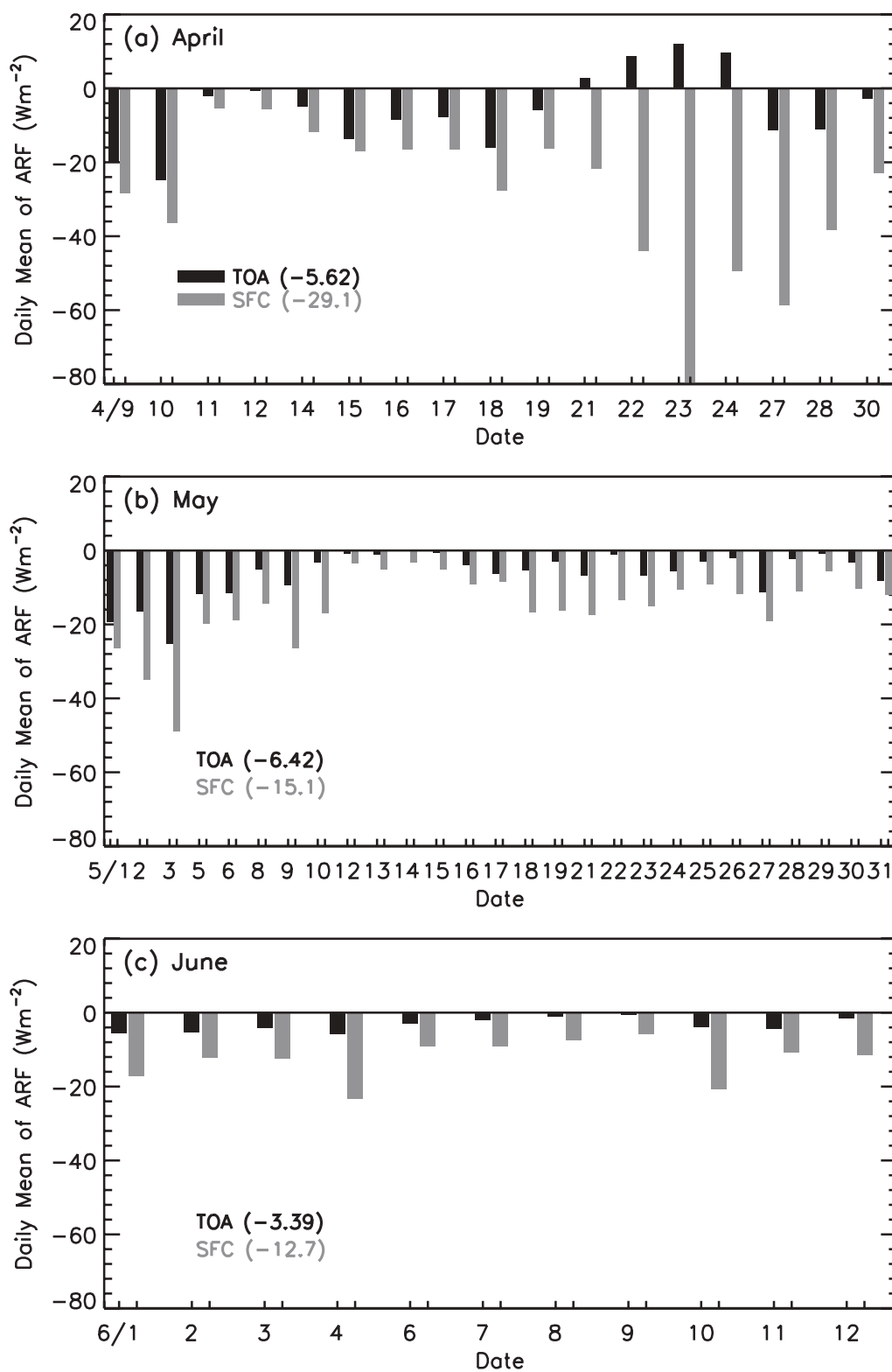


Fig. 11. Daily average values of aerosol direct radiative forcing at the surface (gray bars) and TOA (black bars) at Dunhuang during (a) April, (b) May, and (c) June, 2012.

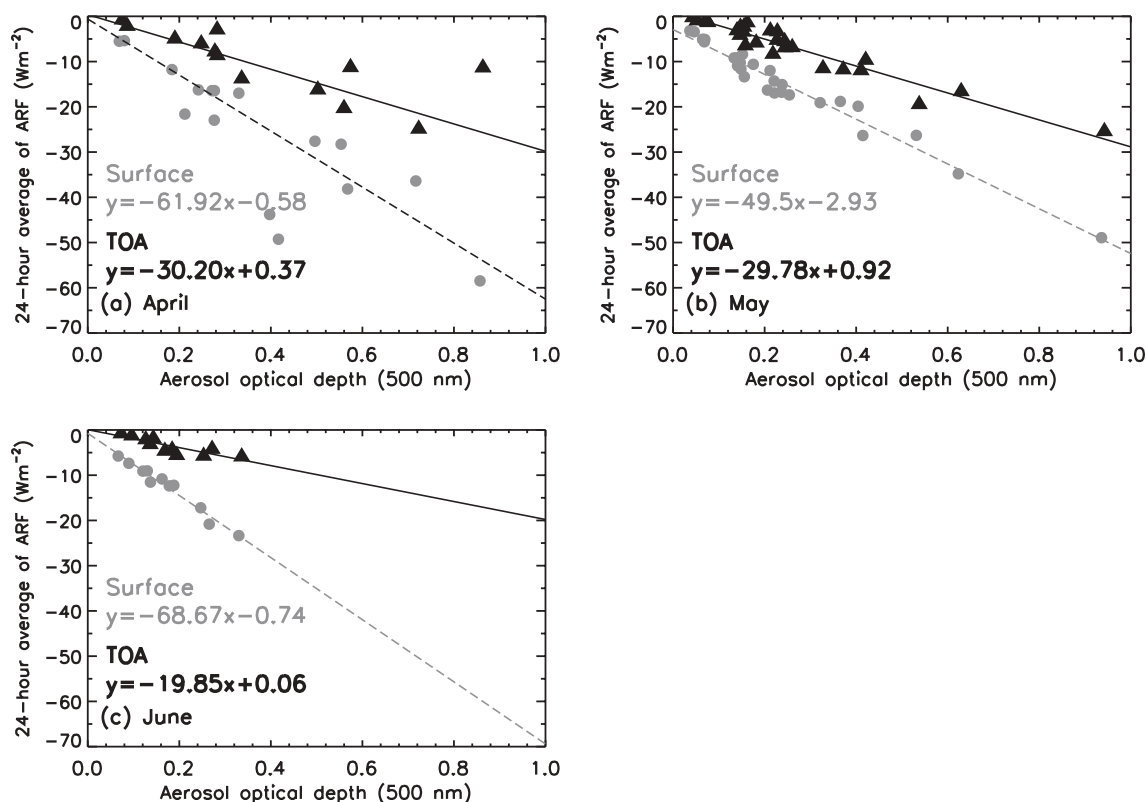


Fig. 12. Correlations between daily mean aerosol direct radiative forcing and AOD₅₀₀ at the surface (gray circle) and TOA (black triangle) at Dunhuang from April to June, 2012.

mated dust ARFs at the surface of a semi-desert area in northwest China range from -35.8 to -7.9 W m⁻² (Ge et al. 2010) and those at three sites in East Asia range from -43 to -13 W m⁻² (Kim et al. 2005). Although these results are higher than ours, the comparisons are favorable. In our study, the monthly mean ARF at the surface was (-29.1 ± 19.8) W m⁻², (-15.1 ± 9.7) W m⁻², and (-12.7 ± 5.5) W m⁻² in April, May, and June, respectively. The overall average surface ARF was (-19.0 ± 14.8) W m⁻², approximately 1.7 times of the global average (-11.0 ± 2) W m⁻² reported by Kim and Ramana (2008). The mean ARF values at the TOA were (-5.6 ± 10.2) W m⁻², (-6.4 ± 6.2) W m⁻², and (-3.4 ± 1.9) W m⁻² (total average = -5.6 ± 7.2 W m⁻²), from which the forcing values of the atmosphere in April, May, and June were determined as (23.5 ± 24.8) W m⁻², (8.7 ± 5.2) W m⁻², and (9.3 ± 4.3) W m⁻², respectively. High surface ARFs coincide with large AOD values. Yu et al. (2006) integrated above-land satellite retrievals with model simulations, and

obtained global average ARFs of (-4.9 ± 0.7) W m⁻², and (-11.8 ± 1.9) W m⁻² at the TOA and surface, respectively. Our results demonstrate that the aerosols in the Dunhuang area are slightly cooled at the TOA and moderately heated in the atmosphere under clear-sky conditions.

Figure 12 plots the correlations between the daily mean ARF and the AOD₅₀₀ at the surface and the TOA throughout the study period. At the surface, the slopes of the best linear fits are -61.9 , -49.5 , and -68.7 in April, May, and June, respectively. The data points are closely spaced in May and June, suggesting that the aerosol composition remained relatively stable over the Dunhuang region during the spring of 2012. Scattering points may partly arise from the wide monthly variations in SSA and ASY (Lee et al. 2007). At the TOA, the slopes of the linear fits in April, May, and June are -30.2 , -29.8 , and -19.9 , respectively.

Figure 13 shows scattergrams of the daily mean ARF at the TOA and surface versus the SSA₅₀₀ and imaginary part of the complex refractive index at 500

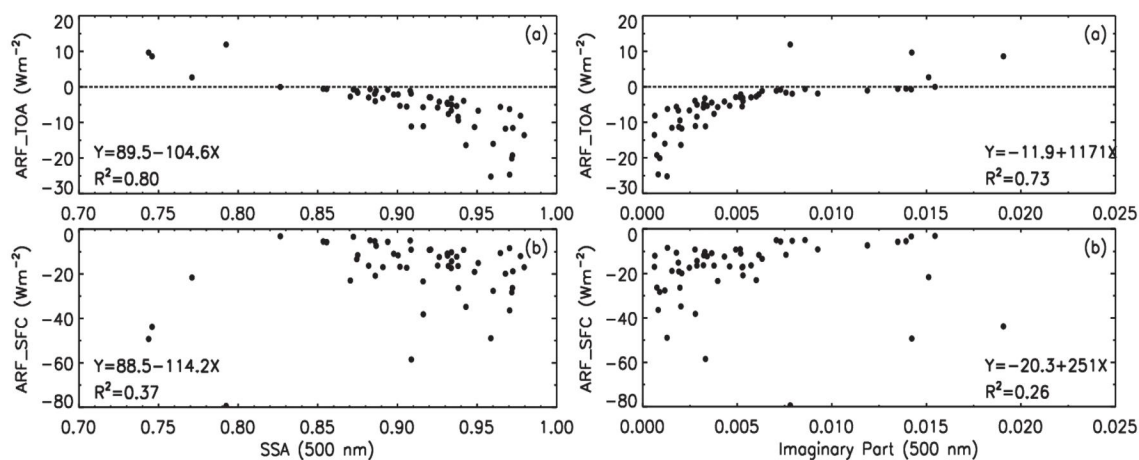


Fig. 13. Daily mean ARFs at the TOA and surface versus SSA_{500} and imaginary part at 500 nm.

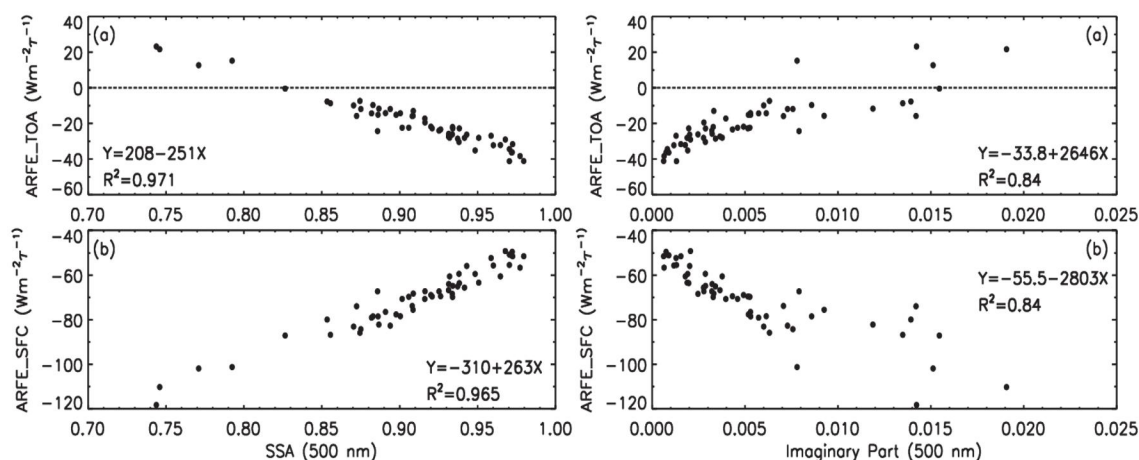


Fig. 14. The same as Fig. 13, but for ARFE.

nm. In these plots, the ARFs at both the TOA and surface appear to decrease with SSA_{500} but increase with the imaginary part at 500 nm. Although few points are plotted, the ARF at the TOA is distinctly positive when SSA_{500} is below 0.85 or when the imaginary part at 500 nm exceeds 0.015. The overall least-squares linear regression is given by $ARF_{TOA} = 89.5 - SSA_{500} \times 104.6$, with a correlation coefficient of 0.80.

We define the daily averaged aerosol radiative forcing efficiency (ARFE) as the diurnal mean ARF divided by the corresponding daily averaged AOD, where we have used the mean AOD at 500 nm. The monthly mean surface ARFEs were (-73.9 ± 11.6)

W m⁻², (-67.4 ± 8.3) W m⁻², and (-74.4 ± 5.4) W m⁻² in April, May, and June, respectively, with an overall average of (-70.8 ± 7.9) W m⁻². Our results are comparable to (-72.2 ± 5.5) W m⁻² estimated from the Indian Ocean Experiment (INDOEX) (Ramanathan 2001b) and (-73.0 ± 9.6) W m⁻² over the AEC-Asia domain, but are slightly larger than in Xianghe (-65.4 ± 4.7) W m⁻² and Beijing (-61.2 ± 3.5) W m⁻² (Li et al. 2010). Kim et al. (2005) investigated three typical sites in East Asia and reported that the total ARFE (ARF per AOD₅₀₀) of Asian dusts ranges from -94 to -65 W m⁻². They claimed that the ARFEs may have been enhanced by mixing with absorptive particles.

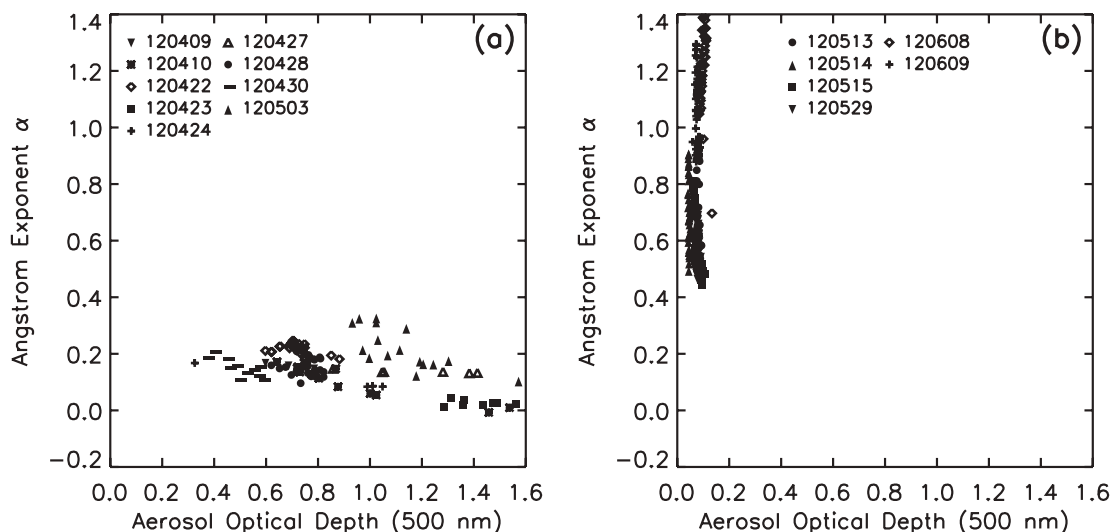


Fig. 15. Scatterplot of the instantaneous Ångström exponent versus aerosol optical depth at 500 nm under (a) dust cases and (b) clear-sky cases, 2012.

Equivalent plots to Fig. 13, but based on the ARFE results, are shown in Fig. 14. The ARFE at the TOA trends to decrease with SSA_{500} and increase with the imaginary part of the refractive index at 500 nm. The ARFE at the surface displays opposite trends. Strong least-squares linear regression relationships are given by $ARFE_{TOA} = 208 - SSA_{500} \times 251$ and $ARFE_{SFC} = -310 + SSA_{500} \times 263$, with correlation coefficients of 0.971 and 0.965, respectively.

5. Dust case study

To investigate the optical properties of dust aerosol, we selected a few days in which dusty events occurred, and compared their optical properties with those obtained under cloudless conditions. Figure 15 shows a remarkable trend, in which the $\alpha_{400-870}$ ranges within 0.0–0.3 while the AOD_{500} is widely spread (0.4–1.6) in the dusty environment. By contrast, under clear-sky conditions, the AOD_{500} varies within 0.0–0.2 while the $\alpha_{400-870}$ varies over a similarly broad range (0.4–1.4). From these two distinct features, we can roughly distinguish the dust from the background aerosol level in northwest China.

Figure 16 displays the size distributions of the aerosol volume under dusty and cloudless conditions. A marked bimodal characteristic is observed under both conditions. However, the coarse-particle mode is dynamic and widely varying in the dusty environment. Under clear skies, the fine-particle and coarse-particle fractions are both significant. As

aforementioned above, the maximum volume value under heavy dust is equal to $0.87 \mu m^3 \mu m^{-2}$, which is considered as the threshold value for eliminating the abnormal data of size distribution. Table 2 lists the volume size distribution under diverse weather conditions (heavy dust, flowing dust, and clear-sky). Interestingly, the peak volumes of the fine-particle fractions are consistently found at $0.173 \mu m$ radius, with volume size spectra ($dV/d\ln r$) of 0.009, 0.007, and $0.004 \mu m^3 \mu m^{-2}$ under heavy dust, light dust, and clear-sky conditions, respectively. However, the respective peak volumes of the coarse-particle fractions appear at radii of 5.29, 1.69, and $2.47 \mu m$, and their corresponding $dV/d\ln r$ values are 0.87, 0.12, and $0.014 \mu m^3 \mu m^{-2}$. Note that the $dV/d\ln r$ values of heavy dust are approximately 7 and 62 times larger than for flowing dust and cloudless cases, respectively, consistent with the aforementioned features.

We define the atmospheric heating rate as the rate of atmospheric temperature change ($\frac{\partial T}{\partial t}$) in a certain layer caused by aerosol-absorbed solar radiation. The heating rate is given by

$$\frac{\partial T}{\partial t} = -\frac{1}{\rho C_p} \frac{\Delta F}{\Delta Z} = \frac{g}{C_p} \frac{\Delta F}{\Delta P} \quad (4)$$

where ρ is the density of air and C_p is the specific heat capacity of the air at constant pressure, $\frac{\Delta F}{\Delta Z}$ is the radiative flux divergence; g is the gravitational acceleration, ΔF is the solar energy absorbed by the aerosol, and ΔP is the atmospheric pressure differ-

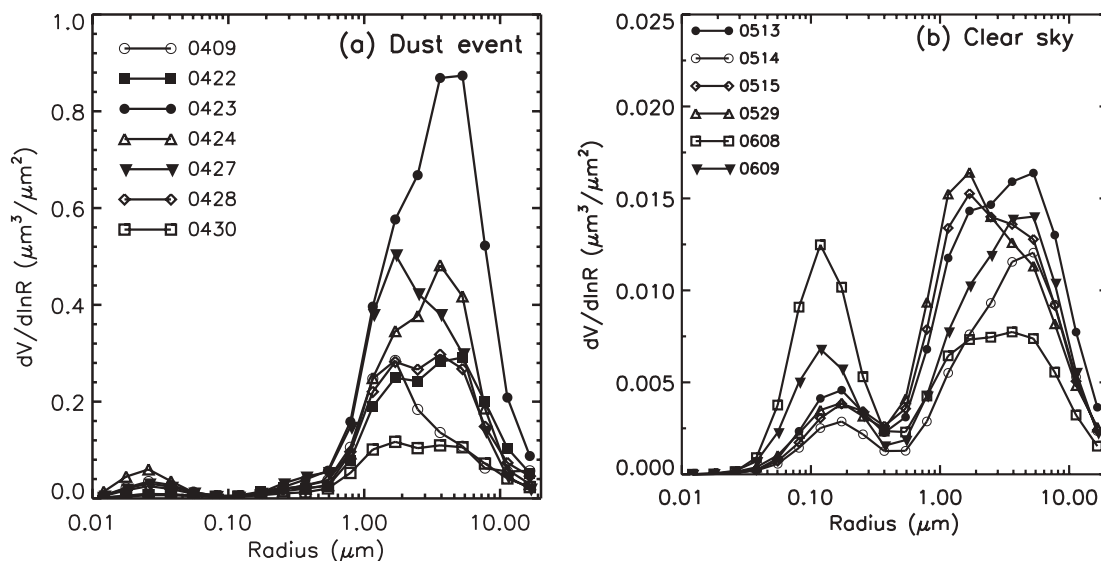


Fig. 16. Retrieved aerosol volume size distributions under (a) dust cases and (b) Clear-sky cases at Dunhuang.

ence between the surface and the tropopause. ΔF is the difference in solar radiation absorbed by the atmosphere in the absence and presence of aerosols.

The daily means of the AOD_{500} , Ångström exponent, SSA_{500} , ARF_{TOA} , ARF_{ATM} , and heating rate on dusty and dust-free days are listed in Table 3. On dusty days, the daily mean AOD_{500} values were 0.27 or higher (maximum = 0.94) and the AEs were less than 0.3. The SSA_{500} values were 0.972, 0.970, 0.909, and 0.958 on April 9, 10, 27, and May 3, respectively. The corresponding values on dust-free days (May 14, 15, 29, and June 8, 9) were 0.908, 0.883, 0.894, 0.887, and 0.856, respectively. We find that the SSA_{500} was increased under dusty conditions, indicating that the dust aerosol in the source region of northwest China is not strongly absorbing. This result is consistent with analyses at the Qira (80.7° E, 37.0°N) site in the Taklimakan Desert (0.91–0.97, Uchiyama et al. 2005). The result is reasonable, because the Dunhuang site is located approximately 400 km east of Taklimakan Desert and is surrounded by the Gobi desert and arid areas with little anthropogenic contamination. Additionally, the heating rate through the whole atmospheric layer ranges from 0.10 to 0.58 K day⁻¹ under dusty conditions. Under clear-sky conditions, the heating rate is much smaller (0.039–0.077 K day⁻¹). From Table 3, we observe that high heating rates coincide with high AOD and high ARF values in the atmosphere. Huang et al. (2009) concluded that dust aerosols in Taklimakan Desert can heat the

atmosphere by up to 1, 2, and 3 K day⁻¹ (daily mean) when the dust layers are light, moderate, and heavy, respectively. According to several investigations, atmospheric heating by absorptive particles may evaporate low-level clouds, reduce the cloud cover and lower the planetary albedo (Ackerman et al. 2000; Wang et al. 2010). Huang et al. (2006, 2010) also pointed out that higher dust aerosol heating over Taklimakan Desert would affect regional climate and monsoon circulation.

6. Summary and conclusions

The SACOL program has sponsored and conducted an intensive field campaign at Dunhuang during the springtime of 2012, when dust storms prevailed over northwest China. In this paper, we investigated the dust aerosol characteristics and its shortwave radiative impact on the regional climate of a source region in northwest China. The analysis was based on sky radiometer measurements and model simulations. The principal findings of this article are summarized below.

The sky radiometer data were excellently fitted to a normal linear Langley plot. From this plot, we determined the calibration constants during the experiment. Although the AOD values were significantly raised in April 2012 by frequent dust events, we acquired the background level AOD (~ 0.04) in Dunhuang under clear-sky conditions. Our results were comparable to the annual mean of 0.029 at Nam Co in the

Table 3. Daily mean values of AOD₅₀₀, Ångström exponent, SSA₅₀₀, ARF_{TOA}, ARF_{ATM}, and heating rate under various dusty and clear-sky cases.

Date	AOD ₅₀₀	AE _{400–870}	SSA ₅₀₀	ARF _{TOA}	ARF _{ATM}	Heating rate	condition
04/09	0.55	0.18	0.972	−20.1	+8.2	0.100	Dust
04/10	0.72	0.12	0.970	−24.7	+11.7	0.143	Dust
04/27	0.86	0.16	0.909	−11.1	+47.3	0.577	Dust
04/30	0.28	0.29	0.870	−2.7	+20.2	0.247	Dust
05/03	0.94	0.28	0.958	−25.2	+23.7	0.289	Dust
06/10	0.27	0.29	0.886	−4.01	+16.8	0.205	Dust
05/14	0.04	0.87	0.908	−0.02	+3.2	0.039	Clear-sky
05/15	0.06	0.72	0.883	−0.62	+4.4	0.054	Clear-sky
05/29	0.07	0.76	0.894	−0.81	+4.8	0.059	Clear-sky
06/08	0.09	1.58	0.887	−1.05	+6.3	0.077	Clear-sky
06/09	0.07	1.43	0.856	−0.58	+5.2	0.063	Clear-sky

central Tibetan Plateau. The overall averaged AOD₅₀₀, $\alpha_{400–870}$, SSA₅₀₀, and ASY₅₀₀ values in Dunhuang throughout the study period were 0.28 ± 0.21 , 0.57 ± 0.35 , 0.91 ± 0.04 , 0.70 ± 0.02 , respectively. The SSA₅₀₀ varied from 0.91 to 0.97 on dusty days and from 0.86 to 0.91 on clear-sky days, indicating that the dust aerosol sourced from northwest China is not strongly absorbing.

The volume size distribution (dV/dlnr) exhibited an apparent bimodal shape throughout the spring months, with a fine-particle mode of radius 0.2–0.3 μm and a coarse particle mode of radius 2–4 μm . The monthly average dV/dlnr of the coarse particles dramatically varied, whereas that of the fine fraction remained comparatively stable. This suggests that coarse particles dominated the aerosol during the spring months at Dunhuang.

An excellent radiative closure experiment was performed, in which the simulated results were compared with ground-based and satellite observations. The results of the SBDART model supported the reasonableness of the parameters in this study (namely, AOD, SSA, ASY, the Ångström exponent, the columnar precipitable water, ozone amount, and spectral surface reflectance).

Aerosol shortwave direct radiative forcing (ARF) was estimated at the TOA, surface, and in the atmosphere. The daily mean ARFs were largely negative at the surface (−79.4 to −3.2 W m^{-2}) and moderately positive in the atmosphere (2.2 to 25.1 W m^{-2}). This situation indicates strong surface cooling and moderate warming in the atmosphere. The relations between the diurnal ARF and AOD₅₀₀ at the surface and at the TOA indicate that aerosol composition remained relatively stable at Dunhuang throughout the

spring of 2012. The ARF at the TOA was positive for SSA₅₀₀ less than 0.85 or when the imaginary part at 500 nm exceeded 0.015.

The monthly average ARFEs (ARF per AOD₅₀₀) at the surface were $(-73.9 \pm 11.6) \text{ W m}^{-2}$, $(-67.4 \pm 8.3) \text{ W m}^{-2}$, and $(-74.4 \pm 5.4) \text{ W m}^{-2}$ in April, May, and June, respectively, with an overall average of $(-70.8 \pm 7.9) \text{ W m}^{-2}$. Our results are consistent with those of previous investigations in East Asia and India domains. The ARFE at the TOA tended to decrease with SSA₅₀₀ and increase with the imaginary part at 500 nm.

Acknowledgments

SACOL was sponsored by Lanzhou University through 985 Program. This work was jointly supported by the National Basic Research Program of China (2012CB955302) and National Science Foundation of China under grant 41305025, 41175134, 41105110. The Fundamental Research Funds for the Central Universities lzujbky-2013-207 and lzujbky-2013-ct05, and the Developmental Program of Changjiang Scholarship and Research Team (IRT1018). The authors would like to express special thanks to Prof. Shi Guangyu's (Institute of Atmospheric Physics, Chinese Academy of Science) great help and support. We are grateful to OpenCLASTR project for supplying SKYRAD software. We are thankful for China Meteorological Administration to provide the Climate Standard Value data. BRDF/TOMS/CERES data supplied by NASA are greatly appreciated. We would also like to thank all anonymous reviewers for their constructive and insightful comments. Part of this research was accomplished while the first author was hosted by the CERES of

Chiba University as a visiting scientist.

References

- Ackerman, A. S., O. B. Toon, D. E. Stevens, A. J. Heymsfield, V. Ramanathan, and E. J. Welton, 2000: Reduction of tropical cloudiness by soot. *Science*, **288**, 1042–1047.
- Bi, J., J. Huang, Q. Fu, X. Wang, J. Shi, W. Zhang, Z. Huang, and B. Zhang, 2011: Toward characterization of the aerosol optical properties over Loess Plateau of Northwestern China. *J. Quant. Spectrosc. Radiat. Transfer*, **112**, 346–360.
- Bi, J., J. Huang, Q. Fu, J. Ge, J. Shi, T. Zhou, and W. Zhang, 2013: Field measurement of clear-sky solar irradiance in Badain Jaran Desert of Northwestern China. *J. Quant. Spectrosc. Radiat. Transfer*, **122**, 194–207.
- Bhartia, P. K., J. Herman, R. D. McPeters, and O. Torres, 1993: Effect of Mount Pinatubo aerosols on total ozone measurements from backscatter ultraviolet (BUV) experiments. *J. Geophys. Res.*, **98**, 18547–18554.
- Campanelli, M., V. Estelles, C. Tomasi, T. Nakajima, V. Malvestuto, and J. A. Martinez-Lozano, 2007: Application of the SKYRAD improved langley plot method for the in situ calibration of CIMEL sun-sky photometers. *Appl. Opt.*, **46**, 2688–2702.
- Dubovik, O., B. N. Holben, T. Lapyonok, A. Sinyuk, M. I. Mishchenko, P. Yang, and I. Slutsker, 2002a: Non-spherical aerosol retrieval method employing light scattering by spheroids. *Geophys. Res. Lett.*, **29**, 1415, doi:10.1029/2001GL014506.
- Dubovik, O., B. N. Holben, T. F. Eck, A. Smirnov, Y. J. Kaufman, M. D. King, D. Tanre, and I. Slutsker, 2002b: Variability of absorption and optical properties of key aerosol types observed in worldwide locations. *J. Atmos. Sci.*, **59**, 590–608.
- Eck, T. F., B. N. Holben, J. S. Reid, O. Dubovik, A. Smirnov, N. T. O'Neill, I. Slutsker, and S. Kinne, 1999: Wavelength dependence of the optical depth of biomass burning, urban and desert dust aerosols. *J. Geophys. Res.*, **104**, 31333–31349.
- Gao Z., J. Bi, and J. Huang, 2013: Analysis on aerosol optical property over Northern China from AERONET/SKYNET observations. *Plateau. Meteor.*, **32**: 888–912 (in Chinese).
- Ge J., J. Su, T. P. Ackerman, Q. Fu, J. Huang, and J. Shi, 2010: Dust aerosol optical properties retrieval and radiative forcing over northwestern China during the 2008 China-U.S. joint field experiment. *J. Geophys. Res.*, **115**, D00K12, doi:10.1029/2009JD013263.
- Hansen, J., M. Sato, and R. Ruedy, 1997: Radiative forcing and climate response. *J. Geophys. Res.*, **102**, 6831–6864.
- Hess, M., P. Koepke, and I. Schult, 1998: Optical properties of aerosols and clouds: The software package OPAC. *Bull. Amer. Meteor. Soc.*, **79**, 831–844.
- Huang, J., P. Minnis, B. Lin, T. Wang, Y. Yi, Y. Hu, S. Sun-Mack, and K. Ayers, 2006: Possible influences of Asian dust aerosols on cloud properties and radiative forcing observed from MODIS and CERES. *Geophys. Res. Lett.*, **33**, L06824, doi:10.1029/2005GL024724.
- Huang, J., P. Minnis, Y. Yi, Q. Tang, X. Wang, Y. Hu, Z. Liu, K. Ayers, C. Trepte, and D. Winker, 2007: Summer dust aerosols detected from CALIPSO over the Tibetan Plateau. *Geophys. Res. Lett.*, **34**, L18805, doi:10.1029/2007GL029938.
- Huang, J., P. Minnis, B. Chen, Z. Huang, Z. Liu, Q. Zhang, Y. Yi, and J. K. Ayers, 2008a: Long-range transport and vertical structure of Asian dust from CALIPSO and surface measurements during PACDEX. *J. Geophys. Res.*, **113**, D23212, doi:10.1029/2008JD010620.
- Huang, J., W. Zhang, J. Zuo, J. Bi, J. Shi, X. Wang, Z. Chang, Z. Huang, S. Yang, B. Zhang, G. Wang, G. Feng, J. Yuan, L. Zhang, H. Zuo, S. Wang, C. Fu, and J. Chou, 2008b: An overview of the semi-arid climate and environment research observatory over the Loess Plateau. *Adv. Atmos. Sci.*, **25**, 906–921.
- Huang, J., Fu, Q., J. Su, Q. Tang, P. Minnis, Y. Hu, Y. Yi, and Q. Zhao, 2009: Taklimakan dust aerosol radiative heating derived from CALIPSO observations using the Fu-Liou radiation model with CERES constraints. *Atmos. Chem. Phys.*, **9**, 4011–4021.
- Huang, J., P. Minnis, H. Yan, Y. Yi, B. Chen, L. Zhang, and J. K. Ayers, 2010: Dust aerosol effect on semi-arid climate over Northwest China detected from A-Train satellite measurements. *Atmos. Chem. Phys.*, **10**, 6863–6872.
- Huang, Z., J. Huang, J. Bi, G. Wang, W. Wang, Q. Fu, Z. Li, S.-C. Tsay, and J. Shi, 2010: Dust aerosol vertical structure measurements using three MPL lidars during 2008 China-U.S. joint dust field experiment. *J. Geophys. Res.*, **115**, D00K15, doi:10.1029/2009JD013273.
- Huebert, B. J., T. Bates, P. B. Russell, G. Shi, Y. J. Kim, K. Kawamura, G. Carmichael, and T. Nakajima, 2003: An overview of ACE-Asia: Strategies for quantifying the relationships between Asian aerosols and their climatic impacts. *J. Geophys. Res.*, **108**, 8633, doi:10.1029/2003JD003550.
- IPCC, 2007: *Climate Change 2007: The Physical Science Basis*. Solomon, S., D. Qin, M. Manning, Z. Chen, M. Marquis, K. B. Averyt, M. Tignor, and H. L. Miller (eds.), Contribution of the Working Group I to the Fourth Assessment Report of the Intergovernmental Panel on Climate Change. Cambridge University Press, Cambridge, United Kingdom and New York, NY, USA.
- Kasten, F., and A. T. Young, 1989: Revised optical air mass tables and approximation formula. *Appl. Opt.*, **28**, 4735–4738.
- Kaufman, Y. J., A. Gitelson, A. Karnieli, E. Ganor, R. S.

- Fraser, T. Nakajima, S. Mattoo, and B. N. Holben, 1994: Size distribution and scattering phase function of aerosol particles retrieved from sky brightness measurements, *J. Geophys. Res.*, **99**, 10341–10356.
- Kaufman, Y. J., I. Koren, L. A. Remer, D. Rosenfeld, and Y. Rudich, 2005: The effect of smoke, dust, and pollution aerosol on shallow cloud development over the Atlantic Ocean. *Proc. Natl. Acad. Sci. U.S.A.*, **102**, 11207–11212.
- Kim, D., and V. Ramanathan, 2008: Solar radiation budget and radiative forcing due to aerosols and clouds. *J. Geophys. Res.*, **113**, D02203, doi:10.1029/2007JD008434.
- Kim, D.-H., B. J. Sohn, T. Nakajima, and T. Takamura, 2005: Aerosol radiative forcing over East Asia determined from ground-based solar radiation measurements. *J. Geophys. Res.*, **110**, D10S22, doi:10.1029/2004JD004678.
- Khatri, P., and T. Takamura, 2009: An algorithm to screen cloud-affected data for sky radiometer data analysis. *J. Meteor. Soc. Japan*, **87**, 189–204.
- Lee, K.-H., Z. Li, M. S. Wong, J. Xin, W.-M. Hao, and F. Zhao, 2007: Aerosol single scattering albedo estimated across China from a combination of ground and satellite measurements. *J. Geophys. Res.*, **112**, D22S15, doi:10.1029/2007JD009077.
- Li, Z., H. Chen, M. Cribb, R. Dickerson, B. Holben, C. Li, D. Lu, Y. Luo, H. Maring, G. Shi, S.-C. Tsay, P. Wang, Y. Wang, X. Xia, Y. Zheng, T. Yuan, and F. Zhao, 2007a: Preface to special section on East Asian Studies of Tropospheric Aerosols: An International Regional Experiment (EAST-AIRE). *J. Geophys. Res.*, **112**, D22S00, doi:10.1029/2007JD008853.
- Li, Z., X. Xia, M. Cribb, W. Mi, B. Holben, P. Wang, H. Chen, S.-C. Tsay, T. F. Eck, F. Zhao, E. G. Dutton, and R. Dickerson, 2007b: Aerosol optical properties and their radiative effects in northern China. *J. Geophys. Res.*, **112**, D22S01, doi:10.1029/2006JD007382.
- Li, Z., K.-H. Lee, Y. Wang, J. Xin, and W.-M. Hao, 2010: First observation-based estimates of cloud-free aerosol radiative forcing across China. *J. Geophys. Res.*, **115**, D00K18, doi:10.1029/2009JD013306.
- Li, Z., C. Li, H. Chen, S.-C. Tsay, B. Holben, J. Huang, B. Li, H. Maring, Y. Qian, G. Shi, X. Xia, Y. Yin, Y. Zheng, and G. Zhuang, 2011: East Asian Studies of Tropospheric Aerosols and their Impact on Regional Climate (EAST-AIRC): An overview. *J. Geophys. Res.*, **116**, D00K34, doi:10.1029/2010JD015257.
- Liou, K. N., 2002. *An Introduction to Atmospheric Radiation*. *Int. Geophys. Ser.*, **84**, Academic Press, CA, USA, 593 pp.
- Liu, Y., J. Huang, G. Shi, T. Takamura, P. Khatri, J. Bi, J. Shi, T. Wang, X. Wang, and B. Zhang, 2011: Aerosol optical properties and radiative effect determined from sky-radiometer over Loess Plateau of Northwest China. *Atmos. Chem. Phys.*, **11**, 11455–11463.
- Mishchenko, M. I., L. D. Travis, R. A. Kahn, and R. A. West, 1997: Modeling phase functions for dust-like Tropospheric aerosol using a shape mixture of randomly oriented polydisperse spheroids, *J. Geophys. Res.*, **102**, 16831–16847.
- Mikami, M., G. Y. Shi, I. Uno, S. Yabuki, Y. Iwasaka, M. Yasui, T. Aoki, T. Y. Tanaka, Y. Kurosaki, K. Masuda, A. Uchiyama, A. Matsuki, T. Sakai, T. Takemi, M. Nakawo, N. Seino, M. Ishizuka, S. Satake, K. Fujita, Y. Hara, K. Kai, S. Kanayama, M. Hayashi, M. Du, Y. Kanai, Y. Yamada, X. Y. Zhang, Z. Shen, H. Zhou, Q. Abe, T. Nagai, Y. Tsutsumi, M. Chiba, and J. Suzuki, 2006: Aeolian dust experiment on climate impact: An overview of Japan-China joint project ADEC. *Global Planet. Change*, **52**, 142–172.
- Moody, E. G., M. D. King, S. Platnick, C. B. Schaaf, and F. Gao, 2005: Spatially complete global spectral surface albedos: Value-added datasets derived from Terra MODIS land products. *IEEE Trans. Geosci. Remote Sens.*, **43**, 144–158.
- Nakajima, T., G. Tonna, R. Rao, P. Boi, Y. Kaufman, and B. Holben, 1996: Use of sky brightness measurements from ground for remote sensing of particulate polydispersions. *Appl. Opt.*, **35**, 2672–2686.
- Nakajima, T., M. Sekiguchi, T. Takemura, I. Uno, A. Higurashi, D. Kim, B. J. Sohn, S.-N. Oh, T. Y. Nakajima, S. Ohta, I. Okada, T. Takamura, and K. Kawamoto, 2003: Significance of direct and indirect radiative forcings of aerosols in the East China Sea region. *J. Geophys. Res.*, **108**, 8658, doi:10.1029/2002JD003261.
- Pandithurai, G., S. Dipu, K. K. Dani, S. Tiwari, D. S. Bisht, P. C. S. Devara, and R. T. Pinker, 2008: Aerosol radiative forcing during dust events over New Delhi, India. *J. Geophys. Res.*, **113**, D13209, doi:10.1029/2008JD009804.
- Ramanathan, V., P. J. Crutzen, J. T. Kiehl, and D. Rosenfeld, 2001a: Aerosols, climate, and the hydrological cycle. *Science*, **294**, 2119–2124.
- Ramanathan, V., P. J. Crutzen, J. Lelieveld, A. P. Mitra, D. Althausen, J. Anderson, M. O. Andreae, W. Cantrell, G. R. Cass, C. E. Chung, A. D. Clarke, J. A. Coakley, W. D. Collins, W. C. Conant, F. Dulac, J. Heintzenberg, A. J. Heymsfield, B. Holben, S. Howell, J. Hudson, A. Jayaraman, J. T. Kiehl, T. N. Krishnamurti, D. Lubin, G. McFarquhar, T. Novakov, J. A. Ogren, I. A. Podgorny, K. Prather, K. Priestley, J. M. Prospero, P. K. Quinn, K. Rajeev, P. Rasch, S. Rupert, R. Sadourny, S. K. Satheesh, G. E. Shaw, P. Sheridan, and F. P. J. Valero, 2001b: Indian Ocean experiment: An integrated analysis of the climate forcing and effects of the great Indo-Asian haze. *J. Geophys. Res.*, **106**, 28371–28398.
- Ricchiazzi, P., S. Yang, C. Gautier, and D. Sowle, 1998: SBDART: A research and teaching software tool for

- plane-parallel radiative transfer in the Earth's atmosphere. *Bull. Amer. Meteor. Soc.*, **79**, 2101–2114.
- Shao, Y., K. Wyrwoll, A. Chappell, J. Huang, Z. Lin, G. McTainsh, M. Mikami, T. Tanaka, X. Wang, and S. Yoon, 2011: Dust cycle: An emerging core theme in Earth system science. *Aeolian Research*, **2**, 181–204.
- Shi, G.-Y., H. Wang, B. Wang, W. Li, S. Gong, T. Zhao, and T. Aoki, 2005: Sensitivity experiments on the effects of optical properties of dust aerosols on their radiative forcing under clear sky condition. *J. Meteor. Soc. Japan*, **83A**, 333–346.
- Smirnov, A., B. N. Holben, T. F. Eck, O. Dubovik, and I. Slutsker, 2000: Cloud screening and quality control algorithms for the AERONET data base. *Remote. Sens. Environ.*, **73**, 337–349.
- Takamura, T., T. Nakajima, and SKYNET community group, 2004: Overview of SKYNET and its Activities. *Opt. Pura y Apl.*, **37**, 3303–3308.
- Takamura, T., N. Sugimoto, A. Shimizu, A. Uchiyama, A. Yamazaki, K. Aoki, T. Nakajima, B. J. Sohn, and H. Takenaka, 2007: Aerosol radiative characteristics at Gosan, Korea, during the atmospheric brown cloud East Asian regional experiment 2005. *J. Geophys. Res.*, **112**, D22S36, doi:10.1029/2007JD008506.
- Ohmura, A., E. G. Dutton, B. Forgan, C. Frohlich, H. Gilgen, H. Hegner, A. Heimo, G. Konig-Langlo, B. McArthur, G. Muller, R. Philipona, R. Pinker, C. H. Whitlock, K. Dehne, and M. Wild, 1998: Baseline Surface Radiation Network (BSRN/WCRP): New precision radiometry for climate research. *Bull. Amer. Meteor. Soc.*, **79**, 2115–2136.
- Uchiyama, A., A. Yamazaki, H. Togawa, J. Asano, and G.-Y. Shi, 2005: Single scattering albedo of Aeolian dust as inferred from sky-radiometer and in situ ground-based measurement. *SOLA*, **1**, 209–212.
- Uno, I., K. Eguchi, K. Yumimoto, T. Takemura, A. Shimizu, M. Uematsu, Z. Liu, Z. Wang, Y. Hara, and N. Sugimoto, 2009: Asian dust transported one full circuit around the globe. *Nature Geosci.*, **2**, 557–560.
- Wang, W., J. Huang, P. Minnis, Y. Hu, J. Li, Z. Huang, J. K. Ayers, and T. Wang, 2010: Dusty cloud properties and radiative forcing over dust source and downwind regions derived from A-Train data during the Pacific Dust Experiment. *J. Geophys. Res.*, **115**, D00H35, doi:10.1029/2010JD014109.
- Wang, W., J. Huang, T. Zhou, J. Bi, L. Lin, Y. Chen, Z. Huang, and J. Su, 2013: Estimation of radiative effect of a heavy dust storm over northwest China using Fu-Liou model and ground measurements. *J. Quant. Spectrosc. Radiat. Transfer*, **122**, 114–126.
- Wang, X., J. Huang, R. Zhang, B. Chen, and J. Bi, 2010: Surface measurements of aerosol properties over northwest China during ARM China 2008 deployment. *J. Geophys. Res.*, **115**, D00K27, doi:10.1029/2009JD013467.
- Xia, X., H. B. Chen, and P. C. Wang, 2004: Aerosol properties in a Chinese semiarid region. *Atmos. Environ.*, **38**, 4571–4581.
- Xia, X., Z. Li, B. Holben, P. Wang, T. Eck, H. Chen, M. Cribb, and Y. Zhao, 2007: Aerosol optical properties and radiative effects in the Yangtze Delta region of China. *J. Geophys. Res.*, **112**, D22S12, doi:10.1029/2007JD008859.
- Xia, X., X. Zong, Z. Cong, H. Chen, S. Kang, and P. Wang, 2011: Baseline continental aerosol over the central Tibetan plateau and a case study of aerosol transport from South Asia. *Atmos. Environ.*, **45**, 7370–7378.
- Yang, P., Q. Feng, G. Hong, G. W. Kattawar, W. J. Wiscombe, M. I. Mishchenko, O. Dubovik, I. Laszlo, and I. N. Sokolik, 2007: Modeling of the scattering and radiative properties of nonspherical dust-like aerosols. *J. Aerosol Sci.*, **38**, 995–1014.
- Yang, X., and M. Wenig, 2009: Study of columnar aerosol size distribution in Hong Kong. *Atmos. Chem. Phys.*, **9**, 6175–6189.
- Yu, H., Y. J. Kaufman, M. Chin, G. Feingold, L. A. Remer, T. L. Anderson, Y. Balkanski, N. Bellouin, O. Boucher, S. Christopher, P. DeCola, R. Kahn, D. Koch, N. Loeb, M. S. Reddy, M. Schulz, T. Takemura, and M. Zhou, 2006: A review of measurement-based assessments of the aerosol direct radiative effect and forcing. *Atmos. Chem. Phys.*, **6**, 613–666.
- Zege, E. P., A. P. Ivanov, and I. L. Katsev, 1991: *Image transfer through a scattering medium*. Springer, New York, 349 pp.